Cement and Concrete Composites 132 (2022) 104634

Contents lists available at ScienceDirect

Cement and Concrete Composites

journal homepage: www.elsevier.com/locate/cemconcomp

Behaviour of strain hardening geopolymer composites at elevated temperatures

Choi Lin Chan, Mingzhong Zhang *

Department of Civil, Environmental and Geomatic Engineering, University College London, London, WC1E 6BT, UK

ARTICLE INFO

Keywords:
Alkali-activated materials
Engineered geopolymer composites
Strain-hardening behaviour
Thermal resistance
Microstructure
Damage evolution

ABSTRACT

Strain hardening geopolymer composite (SHGC) is a sustainable fibre-reinforced material that exhibits superior strain-hardening and multiple cracking behaviour under tension. The geopolymer binder synthesised through alkali-activation of aluminosilicate precursors sourced from industrial by-products is chemically stable at elevated temperatures. This paper presents a systematic experimental study on behaviour of fly ash-slag based SHGC reinforced with polyvinyl alcohol (PVA) fibres exposed to elevated temperatures up to 800 °C through weight loss, uniaxial compressive, ultrasonic pulse velocity (UPV) and uniaxial tensile tests as well as thermal analysis using thermogravimetric analysis (TGA), differential scanning calorimetry (DSC) and derivative thermogravimetry (DTG), X-ray diffraction (XRD), scanning electron microscope (SEM) and mercury intrusion porosimetry (MIP). Results indicate that the compressive strength of SHGC is increased until exposure to 250 °C, followed by a decline up to 600 °C and a regain at 800 °C. The strength gain mechanisms include further geopolymerisation that refines the microstructure, fibre bridging action and sintering that densifies the binder gels, while the strength reduction can be attributed to the damage induced by internal moisture removals and evaporation of fibres, decomposition of calcium compounds, and empty channels introduced by vanished fibres. Besides, the SHGC specimens exposed up to 250 °C exhibit high ductility performance with saturated microcracks when subjected to uniaxial tension, whilst those at 105 °C demonstrate the best strain-hardening degree because of the desired fibre-matrix interaction and enhanced matrix strength. Moreover, no spalling can be observed in SHGC due to its relatively porous structure.

1. Introduction

Elevated temperatures can pose serious threats to concrete structures due to mechanical strength loss, spalling and cracking in concrete, depending on the exposure time and temperature [1,2]. The significant damage of concrete structures can result in unpredictable losses of lives and properties, especially when it is difficult to distinguish fire, e.g., underground [3]. Therefore, many efforts have been made to tackle or mitigate these issues by developing advanced materials with enhanced heat resistance and comparable mechanical performance. Geopolymer, also known as alkali-activated material, has been regarded as a sustainable alternative to ordinary Portland cement because of its low carbon emission, which is produced through the polymeric reaction of alkaline activators and aluminosilicate precursors [4,5]. Alkali hydroxides and silicates such as sodium hydroxide (NaOH) and sodium silicate (Na_2SiO_3) are generally used as the alkaline solution in geopolymers [6]. Industrial by-products such as fly ash (FA) and ground granulated blast-furnace slag (GGBS) have been commonly used as suitable raw materials for geopolymers owing to their sufficient composition of silica and alumina as well as wide availability [4,7–9]. FA-based geopolymer has been a promising substitute for cementitious materials because of its superior mechanical properties, durability and fire resistance [10–14].

In recent years, an increasing number of attempts have been made to develop geopolymer as a heat or fire resistant material by assessing its chemistry, microstructure and microscopic properties at high temperatures. A general agreement has been reached that FA-based geopolymers exhibit excellent chemical stability after heat exposure, as opposed to ordinary Portland cement [15–19]. FA-based geopolymers heated up to 1000 °C largely maintained their amorphous structures with minimal crystalline phase changes and had improved compressive strength [15–18,20,21]. The primary mechanism behind this strength gain is the sintering effect that alters the microstructure of FA-based geopolymers at high temperatures. This is because sintering can lead to (1) flow of aluminosilicates that boost the interparticle bonding [16], (2)

* Corresponding author.
E-mail address: mingzhong.zhang@ucl.ac.uk (M. Zhang).

https://doi.org/10.1016/j.cemconcomp.2022.104634
Received 6 September 2021; Received in revised form 21 May 2022; Accepted 12 June 2022
Available online 15 June 2022

densification that increases the gel-to-space ratio [17], and (3) high portion of micropores that allow moisture to leave during heating [21]. However, the reduction in strength was also observed in FA-based geopolymers due to enlarged pores and crack development caused by escaping vapour at elevated temperatures [15,17,18]. The extent of cracking is dependent on the pressure accumulation induced by internal water transport that is highly governed by the pore structure of geopolymers [16,18,22]. Although FA-based geopolymers show superior heat resistance, they require rigorous curing conditions of 60–85 °C to achieve early-strength gain [23–25]. To conquer this problem, GGBS can be added into the FA-based geopolymers to facilitate the formation of reaction products under ambient curing conditions [26–30]. The binding gels in this system are N-A-S-H gels from the FA reaction which improve durability, C-A-S-H gels generated by GGBS activation that enhance mechanical strength and have lower porosity, and N–C-A-S-H gels formed by the calcium incorporation in N-A-S-H gels [31–33]. Depending on the competing thermally induced microstructural evolution, different thermal effects on mechanical properties of FA-GGBS based geopolymers have been reported [34–39]. The reasons for strength loss mainly include: (1) increase in porosity [36], (2) calcite decomposition and decreased thermal stability of N–C-A-S-H gel [35], and (3) crack formation due to thermal strain discrepancy between geopolymer matrix and aggregates [37], while sintering is the main cause of strength regain [34].

Due to the intrinsic brittleness of geopolymer, different fibres including steel, carbon, synthetic and natural fibres were incorporated into geopolymer to obtain desirable mechanical and thermal properties for engineering applications [40]. Strain hardening geopolymer composite (SHGC), also called engineered geopolymer composite (EGC), is a special class of fibre-reinforced geopolymer composite (FRGC) that combines the features of strain hardening cementitious composite (SHCC) or engineered cementitious composite (ECC) and geopolymer. SHCC or ECC is a micromechanics-based designed material with extraordinary strain-hardening and multiple cracking behaviour under tensile loading [41–44]. Synthetic fibres such as polyvinyl alcohol (PVA) fibre and polyethylene (PE) fibre are usually used to reinforce cementitious or geopolymer matrices. The mechanical properties of SHGC made from FA, GGBS, and FA-GGBS based geopolymer reinforced with PVA fibres have been extensively investigated. It was reported that SHGC exhibited excellent ductility performance with a tensile capacity of 3.0–4.5%, a tensile strength of up to 6.8 MPa, and tight crack widths of below 50 μm, whilst maintained sufficient compressive strength of 45.7–102.3 MPa [45–50]. Recently, SHGC with a blended binder system has attracted increasing interest because of its sustainable features, strain-hardening performance under tensile loading and enhanced durability by well-controlled crack widths. However, PVA fibre melts at around 250 °C and decomposes into gases at a temperature above 400 °C, which would affect the properties of SHGC at high temperatures [51–53]. Up to now, only limited studies have explored the effect of elevated temperatures on the behaviour of FRGC [54–58]. It was demonstrated that the bridging effect and strong adhesion between carbon fibre and matrix enhanced the flexural strength and toughness of metakaolin-based geopolymer at high temperatures [58,59]. Masi et al. [60] examined the influences of PVA and basalt fibres on the thermal performance of FA-based geopolymers up to 250 °C and 1000 °C, respectively. They found that PVA fibres sustained the flexural strength of geopolymer up to 150 °C, while basalt fibres increased the flexural strength as sintering contributed to the strong fibre-matrix adhesion beyond 700 °C. Moreover, steel fibre-reinforced geopolymer composites improved their compressive and tensile strengths up to 400 °C, after which they underwent strength losses due to damage of fibres and aggregate-matrix interface [61]. However, most of the studies only focused on typical FRGC while the behaviour of FA-GGBS based SHGC at elevated temperatures has been rarely explored, which would restrain its engineering applications. Thus, it is vital to investigate the changes in engineering properties and microstructural evolution of FA-GGBS based SHGC subjected to elevated temperatures, starting from ambient conditions to high temperatures, which would enable us to better understand the damage evolution and predict the response of SHGC structural elements under thermal/fire exposure.

The main purpose of this study is to systematically investigate the behaviour of PVA fibre reinforced FA-GGBS based SHGC cured at ambient temperature when subjected to elevated temperatures, including room temperature, 105, 250, 400, 600, and 800 °C. A series of tests were conducted to explore the macroscopic engineering properties of SHGC after heat exposure in terms of weight loss, compressive strength, ultrasonic pulse velocity (UPV) and uniaxial tensile behaviour. Afterwards, the thermal behaviour and microstructural characteristics of SHGC against elevated temperatures were examined using thermogravimetric analysis (TGA), differential scanning calorimetry (DSC), derivative thermogravimetry (DTG), X-ray diffraction (XRD), scanning electron microscope (SEM) and mercury intrusion porosimetry (MIP). Finally, the relationships between the macroscopic observations and microstructure evolution of SHGC are discussed in detail based on the experimental results to provide new insights into the underlying mechanisms of damage evolution in SHGC exposed to elevated temperatures.

2. Experimental program

2.1. Raw materials

In this study, low-calcium FA (corresponding to ASTM C618 - 17a [62]) and GGBS were selected as the precursors to synthesise geopolymer, the chemical compositions and particle size distribution of which are presented in Table 1 and Fig. 1, respectively. FA has an average particle size of 19.58 μm and a specific gravity of 2.19, while the average particle size and specific gravity of GGBS are 9.78 μm and 2.90, respectively.

A mixture of sodium hydroxide (NaOH) solution with a molarity of 10 and sodium silicate (Na_2SiO_3) solution with a SiO_2/Na_2O ratio of 3.15 (Na_2O: 8.5 wt%, SiO_2: 26.8 wt%, H_2O: 64.7 wt%) was used as the alkaline activator. The specific gravities of NaOH and Na_2SiO_3 are 1.31 and 1.38, respectively. To achieve acceptable workability of the mixtures and ensure a uniform fibre dispersion, the polycarboxylate-based superplasticiser (SP, Sika®ViscoFlow®3000) was added [47,50,63], the properties of which are presented in Table 2. To limit the fracture toughness and maintain the strain-hardening behaviour of SHGC [58], the silica sand with a specific gravity of 2.66, a mean grain size of 130 μm and a maximum grain size of 250 μm was used in this study, the particle size distribution of which is also shown in Fig. 1.

In this work, PVA fibres (Kuraray Co., Ltd., Japan) were adopted as reinforcement for SHGC, which were coated with 1.2 wt% oil content to control the interfacial properties between matrix and fibres. The thermal analysis of PVA fibres was performed to investigate the effect of elevated temperature on the mass loss and heat flow of fibres. Fig. 2 demonstrates the TGA, DSC, and DTG curves of PVA fibres from ambient temperature to around 600 °C, indicating that the melting point of PVA fibres is 248 °C, with most of the mass loss observed between approximately 250 °C and 475 °C. This was originated from the decomposition of polymeric side chains as the melting and vaporisation process. The final mass loss of PVA fibres was found to be over 94% at 570 °C, which became thermally unstable above 366 °C as the main chain of them decomposed, with a maximum rate of mass loss of 14%/min at this point. The peak at 439 °C corresponds to the degradation point of PVA fibre constituents. More details about the PVA fibres are summarised in Table 3.

2.2. Mix proportions

The mix proportions of SHGC used in this study are given in Table 4, according to the previous studies [47,50,63]. The Na_2SiO_3/NaOH ratio

Table 1
Chemical compositions (wt%) of FA and GGBS.

Oxide	SiO_2	Al_2O_3	Fe_2O_3	CaO	SO_3	MgO	TiO_2	P_2O_5	LOI
FA	57.02	32.35	3.01	2.88	0.41	0.58	1.26	0.20	2.45
GGBS	31.85	17.31	0.34	41.20	1.78	6.13	0.62	0.02	0.39

Note: LOI (Loss on Ignition).

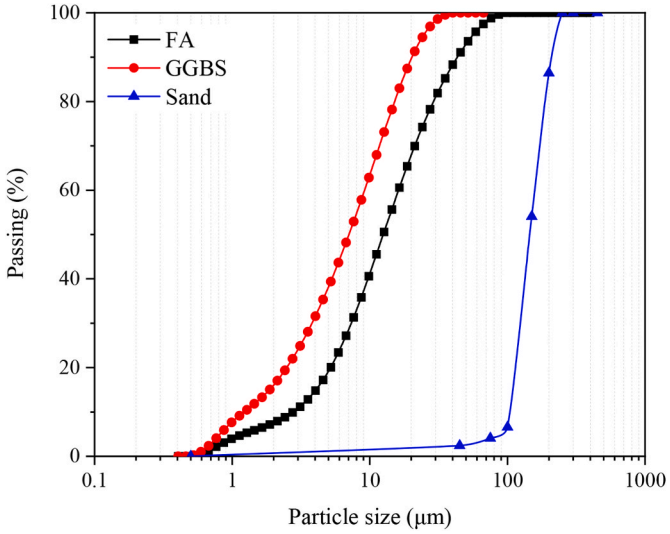

Fig. 1. Particle size distribution FA, GGBS and fine silica sand.

Table 2
Properties of superplasticiser (SP).

Specific gravity (at 20 °C)	pH (25 °C)	Content of chloride ion (%)	Content of alkaline (%)
1.06	4.5 ± 1.0	≤0.1	≤0.25

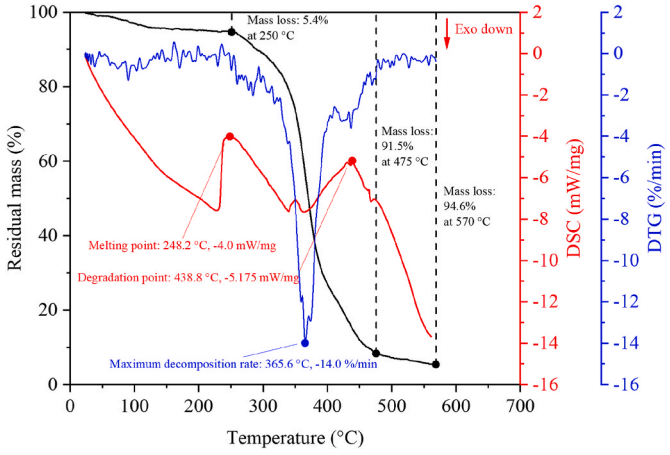

Fig. 2. TGA, DSC and DSC curves of PVA fibre.

Table 3
Characteristics of PVA fibre.

Length (mm)	Diameter (μm)	Elongation at break (%)	Tensile strength (MPa)	Elastic modulus (GPa)	Density (kg/m^3)
12.0	40.0	6.5	1560	41.0	1300

Table 4
Mix proportion of SHGC specimens.

Binder		Silica sand/binder	AL/ binder	SP/ binder	PVA fibre (vol%)
FA	GGBS				
0.8	0.2	0.2	0.45	0.01	2.0

of the alkaline activator was 1.5. The constant fibre dosage was set as 2 vol% for investigation, as the mixtures reinforced with 2 vol% PVA fibres can obtain a flow spread increase of 95 ± 2% as per ASTM C1437-15 [64].

2.3. Sample preparation

The 10 M NaOH solution was first prepared by mixing 400 g NaOH pellets with 1 L of water, which was then stored for 24 h to release heat before the mixing procedures. The mixing process of SHGC began with the drying mixing of FA, GGBS and sand for 1.5 min, followed by the addition of alkaline activator. Afterwards, SP was added after another mixing of 1 min. PVA fibres were then gradually added to ensure even dispersion of fibres in the mixture. The entire mixing process lasted for 9–9.5 min and was conducted in a 20 L planetary mixer with a constant speed of 140 rpm. The fresh mixtures were subsequently poured into different moulds that were placed on the vibrating table for better compaction and removal of entrapped air. All samples were sealed by plastic sheets for 24 h in the room temperature (20 ± 2 °C), which were demoulded and placed under the curing conditions (20 ± 2 °C, 95% relative humidity) for 28 d until the test stage.

2.4. Heating methods

At 28 d, the surfaces of samples were dried under ambient conditions before the samples were heated up to the target temperatures. Herein, the samples were exposed to 6 temperatures, including room temperature, 105, 250, 400, 600, and 800 °C. The heating process was simulated with an electric furnace with a constant heating rate of 10 °C/min that was employed in previous studies and is consistent with ASTM E831 [36,65,66]. As per Refs. [67], the temperature differences between the furnace and the sample centre were less than 1 °C when samples were heated to 1000 °C. Since the maximum temperature was 800 °C, the temperatures were maintained for 2 h to ensure all samples reached a thermal equilibrium state [68]. The tests were carried out after the samples were naturally cooled down to room temperature in the furnace.

2.5. Test methods

2.5.1. Mass loss

The initial mass of 50 mm SHGC cubes (m_0) was measured before the heat exposure and the heated mass (m_1) was then recorded to calculate the mass loss affected by temperature exposure. The mass loss rate (r_m) can be calculated as:

$$r_m = \frac{m_0 - m_1}{m_0} \times 100\% \quad (1)$$

2.5.2. Ultrasonic pulse velocity (UPV)

The UPV test was conducted on 50 × 100 mm SHGC cylinders after

exposure to the target temperatures (i.e., 105, 250, 400, 600 and 800 °C) and cooling down. In UPV test, an ultrasonic pulse passes through the specimen and the transit time is measured. The end surfaces of specimens were polished and flattened before the measurements were taken by a pulse meter (HS-YS403B) with a transducer pair. The UPV tester had a frequency range of 10 kHz −1.5 MHz and a sampling rate of 0.16 μs. For each measurement, sufficient gel was applied on the contact interfaces between the transducers and the specimen. Then, the transducers were held firmly against the opposite surfaces of cylinder until stable readings were obtained. The UPV (v) value of each specimen can be calculated using the travel time (Δt) and the height of polished cylinders (l) as $v = l/\Delta t$.

2.5.3. Uniaxial compressive test

The uniaxial compressive test was performed on SHGC cubes (50 mm × 50 mm × 50 mm) at 28 d, as per ASTM C109/C109M-20b [69]. The maximum load capacity of testing machine was 1000 kN and the loading rate of 0.3 MPa/s, along with the peak sensitivity of 3 kN was set for all specimens. The average compressive strength of three specimens was used for all temperatures in this study.

2.5.4. Uniaxial tensile test

The uniaxial tensile test was carried out on the dog-bone shaped SHGC specimens at 28 d with a loading rate of 0.5 mm/min. The geometry of dog-bone specimen and experimental setup are illustrated in Fig. 3 [70]. During the test, the deformations were measured and recorded using a pair of linear variable displacement transducers (LVDTs) attached at both sides of the central gauge area with a length of 80 mm. The full range of tensile stress-strain relationship and the cracking behaviour were determined with this setup. Herein, the key tensile parameters of SHGC specimens representing tensile properties were obtained from the stress-strain curves, including first-crack strength (f_{fc}), tensile strength (f_t), tensile strain capacity (ε_t), and strain energy, as demonstrated in Fig. 4 with the highlighted parameters. In general, a typical tensile stress-strain curve of SHGC exhibited three

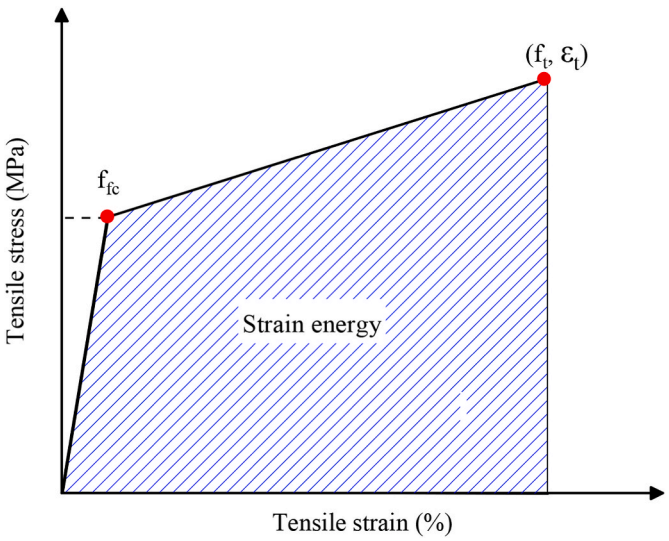

Fig. 4. Typical tensile stress-strain curve and key parameters.

distinct stages, including a linear elastic stage, a strain-hardening stage, and a strain softening stage. Since the curve may show a smooth transition point between the first and second stages, f_{fc} is obtained at the limit of proportionality of elastic stage in case the first stress drop is hard to be identified. Strain energy that is the energy dissipation capacity per unit volume during the strain-hardening stage is adopted as a measure of strain-hardening degree. It was determined by obtaining the total area under the ascending section of the stress-strain curve through integration. At the strain-hardening stage, the number of cracks increases with the development of tensile strain capacity. Hence, the cracking behaviour, including crack numbers, crack widths, and fibre status at the failure section, was determined with a digital microscope (WM401WIFI, Shanghai) to understand the fibre bridging effect and toughening

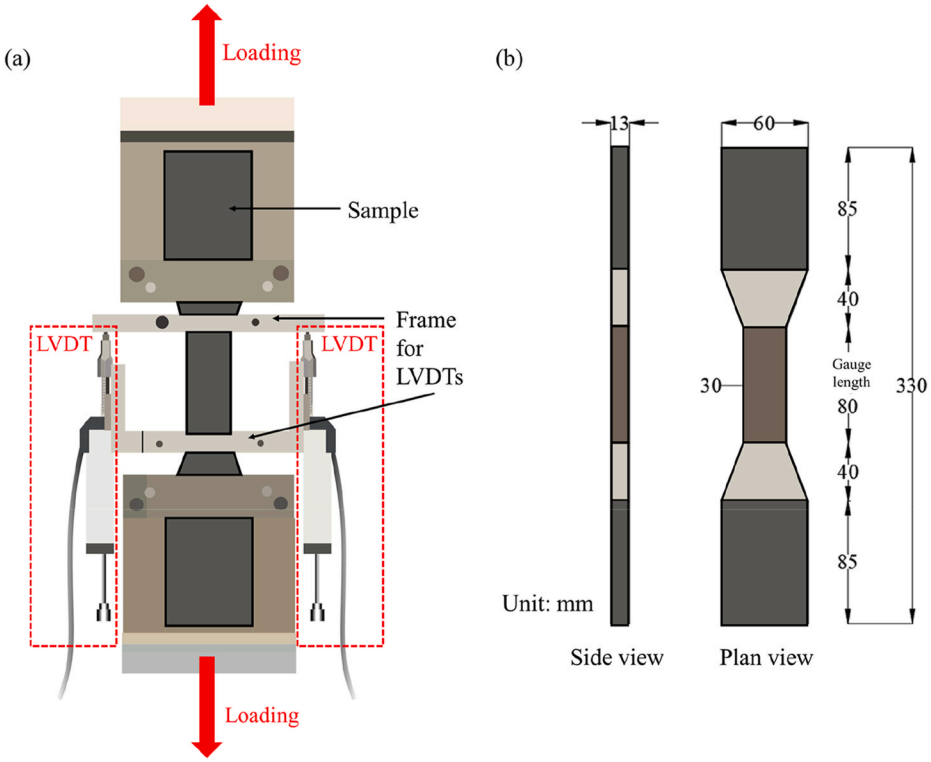

Fig. 3. Uniaxial direct tensile test: (a) test setup; (b) geometry of dog-bone specimen.

mechanisms. The crack patterns within the central area of interest were also captured to illustrate the distribution of cracks.

2.5.5. Thermal analysis

DSC and TGA were conducted to determine the thermal stability of PVA fibre and SHGC. The analysis was carried out on the powered samples using the machine NETZSCH STA 490F5. The gas flow was 50 ml/min, whereas the constant hearing rate was 10 °C/min. The TGA and DSC curves demonstrate the weight loss and the heat transformation of samples at elevated temperatures, respectively. The DTG curve is the derivative of the TGA curve to indicate the rates of weight loss.

2.5.6. X-ray diffractometer (XRD)

The phase stability of SHGC exposed to different temperatures was investigated by means of XRD analysis, which has been widely applied to evaluate the crystallographic structure of SHGC [16,36,71]. The XRD patterns of SHGC samples exposed to different temperatures were collected with the machine MPDDY2094 (PANalytical B.V., Netherlands). The fragments of cubes subjected to compression were utilised for XRD analysis. The data was collected applying a 2θ step size of 0.02°, a scanning rate of 6°/min, and a 2θ up to 90°.

2.5.7. Scanning electron microscope (SEM)

The microstructure evolution of fibres subjected to rising temperatures was examined using the SEM equipment Phenom ProX at one fixed position and relevant bonding at lower magnifications (<1000 ×). Moreover, the fibre-matrix interfaces and matrix behaviour at higher magnifications were captured with the apparatus TESCAN MIRA3. The SHGC samples with dimensions smaller than 100 mm were cut and grounded from cylinders used in UPV tests. Prior to testing in a vacuum, these samples were coated with a layer of gold to eliminate charging effects and optimise image resolution. The tests were carried out on flat sections with an acceleration voltage of 10 kV.

2.5.8. Mercury intrusion porosimetry (MIP)

MIP was employed to characterise the pore structure of SHGC exposed to high temperatures, in terms of porosity and pore size distribution (PSD). To prepare for this test, the specimen fragments obtained from previous tests with sizes smaller than 500 mm^3 were selected. The pore diameters ranging from 0.001 μm to 1000 μm were investigated using pressurised mercury as a non-wetting liquid. In this method, the mercury fills the larger pores first and progresses to the smaller pores as the pressure is applied [72]. This test was carried out using an AutoPore IV 9500 manufactured by Micromeritics Instrument Corporation with a pressure range of up to 414 MPa. The contact angle between the mercury and sample was assumed to be 130°.

3. Results

3.1. Weight loss and visual appearance

Fig. 5 shows the changes of weight loss of SHGC specimens from room temperature to 800 °C relative to their original weights before the heat exposure. Overall, the weight loss of SHGC increased with temperature, while the results obtained from different samples for each mixture were consistent with tiny variations. The weight loss can be attributed to the evaporations of different types of water and PVA fibres in SHGC. The weight reduction reached 2.6% upon 105 °C heating due to the weakly absorbed and free water removals [21]. In the range of 105–250 °C, an apparent sharp decrease in weight with a value of 14.5% took place, which can be mainly ascribed to the escaping tightly absorbed water and chemically bound water in geopolymer gels as the dehydration of amorphous matrix started [73,74]. Due to the presence of calcium in GGBS, the decomposition of calcium-based reaction products (such as C–S–H) also led to an increase in weight loss [75]. Meanwhile, PVA fibres started to melt at 248 °C, which contributed to some degrees of weight loss. Up to this stage, the weight loss associated with the expel of free and structural water could lead to thermal shrinkage, resulting in the formation of cracks inside the SHGC samples [20]. Between 250 °C and 400 °C, the rate of weight loss was slightly decreased, which reached 20.8% at 400 °C. The primary reasons are the melting and evaporation of PVA fibres since 86% weight loss of fibres was observed in this period, accompanied by further dehydroxylation of hydroxy groups in geopolymer [74]. Afterwards, the ongoing dehydration of reaction products and the entire evaporation of PVA fibres were responsible for the weight loss above 400 °C with a significantly reduced rate, resulting in a total loss of 22.6%.

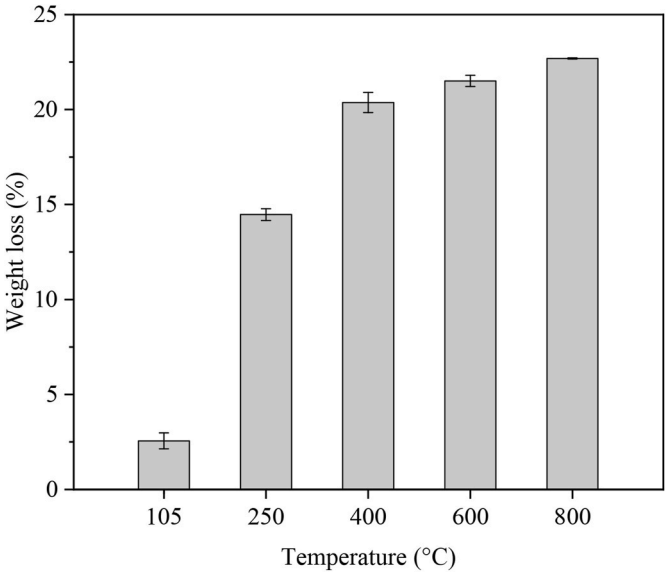

Fig. 5. Weight loss of SHGC exposed to different temperatures.

Fig. 6 demonstrates the images of SHGC samples after exposure to different temperatures. No sign of spalling can be observed in all SHGC specimens. The unexposed SHGC sample was grey at ambient temperature, whilst the brownish degrees of samples increased with the heated temperatures. This can be explained by the oxidation of inherent iron compounds (Fe_2O_3) presented in FA and GGBS particles during heat exposure [18]. After exposed to 250 °C, the SHGC sample became light brown with burnt PVA fibres distributed on its surface. Herein, the colour of PVA fibres turned from white up to 105 °C to golden brown afterwards due to thermal decomposition. Then, the fibres completely disappeared after 400 °C with few dark-brown residues left on the samples exposed to higher temperatures. No surface cracks can be observed on the samples subjected to below 800 °C. However, apparent macrocracks developed in the sample at 800 °C, which can be ascribed to the rise of thermal stresses and rapid shrinkage in the sample [15,76].

3.2. Compressive strength

Fig. 7 displays the failure modes of heated SHGC under uniaxial compression. The samples remained their original shapes with visible cracks developed in the cubes at room temperature, 105, and 250 °C, whilst those exposed to 400, 600, and 800 °C experienced crushing failure with flying fragments. The reinforced fibres provided extra energy to curtail the lateral tensile stress within the sample and prevented the propagation of cracks, even when they partially melted at 250 °C [77]. Above 400 °C, the PVA fibres completely degraded, resulting in the loss of crack-bridging capacity in the specimens and thus the brittle failures occurred at higher temperatures.

The average compressive strength of SHGC cured at ambient temperature for 28 d after exposure to elevated temperatures is shown in Fig. 8. The average compressive strength of SHGC at ambient

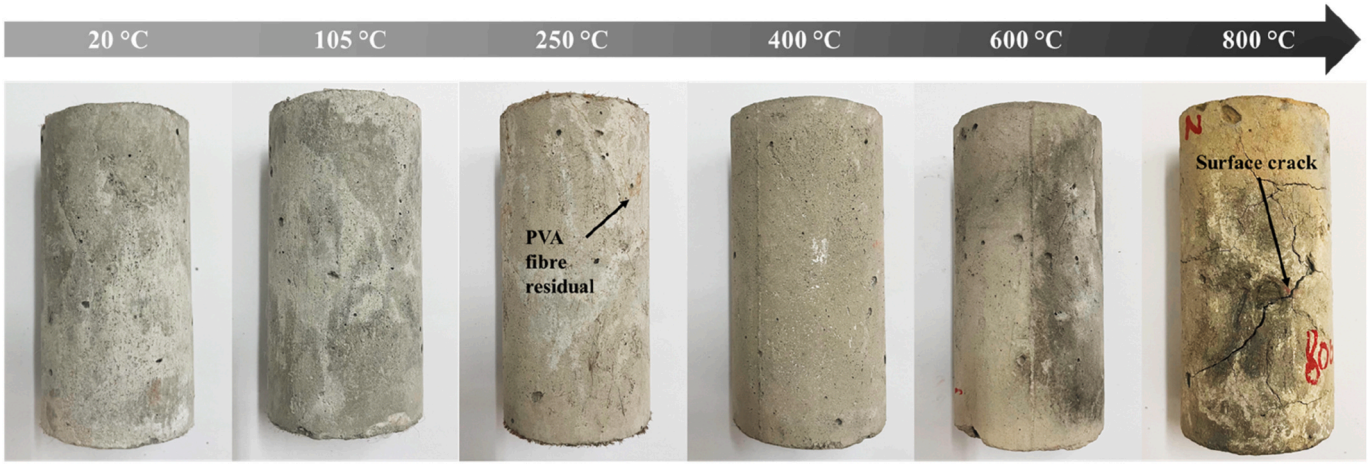

Fig. 6. Visual appearance of SHGC exposed to different temperatures.

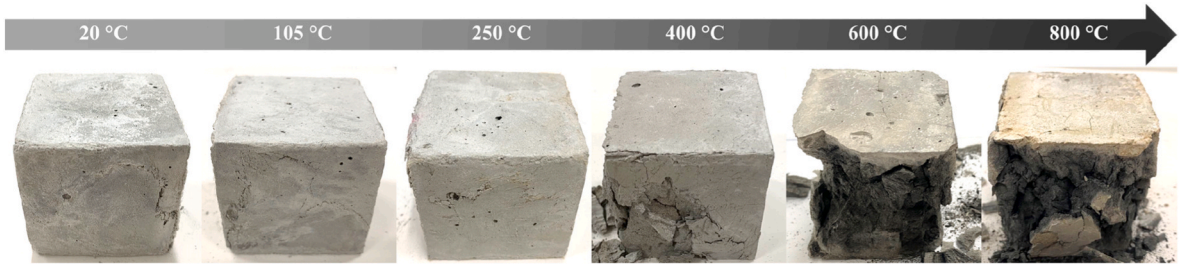

Fig. 7. Compressive failure modes of SHGC exposed to different temperatures.

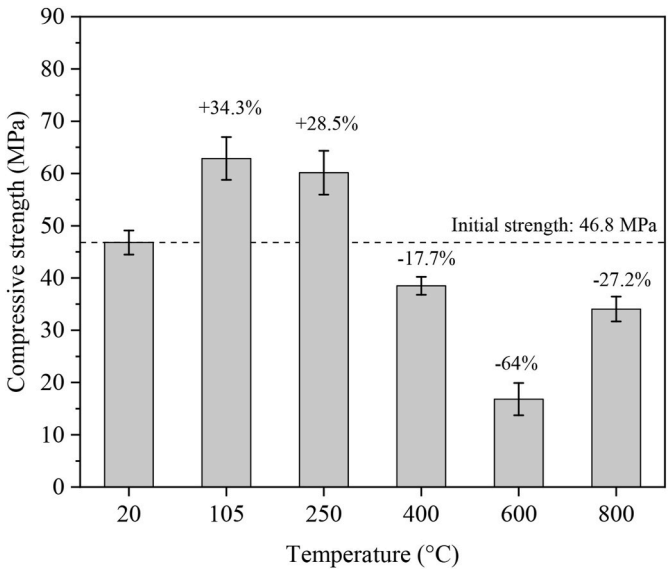

Fig. 8. Compressive strength of SHGC exposed to different temperatures.

temperature was 46.8 MPa and was increased by 34.3% compared to the unheated SHGC with a value of 63.3 MPa after initial heating up to 105 °C. It is indicated that the heat treatment can facilitate the activation of unreacted FA particles presented in SHGC and led to strength enhancement [23,78]. A slight decrease of 5.8% was observed for compressive strength of SHGC after exposure to 200 °C, though still 28.5% higher than the initial strength. Following this, a significant drop of 52.1% in compressive strength at 400 °C can be observed as all fibres have melted. The retained strength of samples at 600 °C reached the lowest point at 16.83 MPa, which was 36% of the unexposed strength. However, after the exposure to 800 °C, the compressive strength of samples exhibited a twofold increase compared to that of 600 °C. The strength variations can be explained by different processes within the samples that led to the two contradiction trends. The increase in compressive strength at high temperatures is the result of further geopolymerisation and sintering effects in geopolymer matrix, along with the crack-bridging effect of PVA fibres. In contrast, the mechanical properties of SHGC at elevated temperatures can be reduced due to the pore pressure effects caused by the removals of water and hydroxyls, empty channels and microcracks induced by the melting PVA fibres, and growth of porous structure in the matrix [18,36,56].

3.3. Ultrasonic pulse velocity

UPV is a non-destructive method used to evaluate the porosity and permeability affected by the voids in cementitious materials, which is usually applied to assess concrete strength and quality [79,80]. It was also found that UPV values of geopolymers can be correlated to their compressive strength with an adequate level of confidence [81–83]. Fig. 9 illustrates the UPV as an indicator of uniformity of SHGC exposed at elevated temperatures, indicating that the UPV values of SHGC exposed to elevated temperatures exhibit a similar trend with the compressive strength results presented in Fig. 8. The ultrasonic speed of SHGC was 2800 m/s at ambient temperature, with slight increases when temperatures rose to 105 °C and 250 °C. This suggests that although the water evaporation in geopolymer matrix increased as observed in the weight loss, the voids within the samples reduced due to the further geopolymerisation and a denser microstructure.

In addition, the discrepancies of strength results between ambient temperature and 100 °C were more significant than that of UPV. This suggests that the compressive strength was enhanced due to the confining effect of PVA fibres as more energy is required to bridge cracks

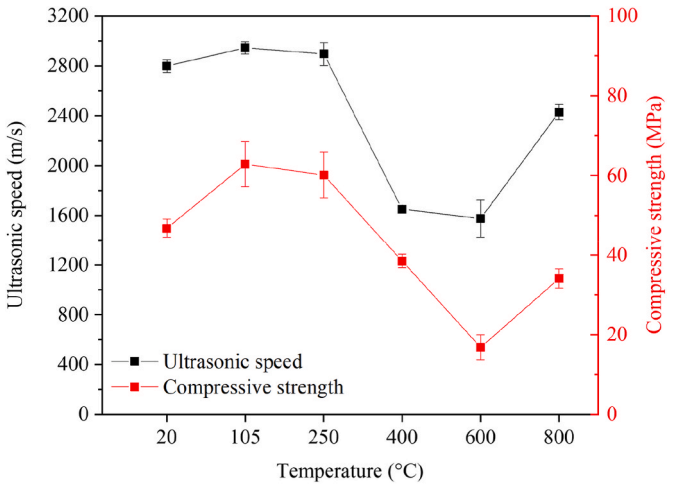

Fig. 9. Comparison of UPV values and compressive strength of SHGC exposed to different temperatures.

[77]. Afterwards, a notable reduction of UPV implied that serious damages existed in the specimens due to the effect of 400 °C, which is consistent with the strength results. The melting and degradation process of PVA fibres happened between 250 °C and 475 °C, resulting in the formation of microscopic channels and microcracks in the specimens. The increment of porosity and defects in SHGC after exposure to high temperatures increased the transport distance of pulse waves and hence lowered the UPV values. This trend continued to 600 °C, followed by an increase from 1570 m/s to 2430 m/s when the temperature rose from 600 °C to 800 °C. This finding agrees well with the compressive strength results, suggesting that the microstructure became denser at 800 °C. The correlation between UPV and compressive strength of SHGC exposed to elevated temperatures is shown in Fig. 10. There exists a linear relationship with a correlation coefficient of about 0.72, indicating that UPV can be an acceptable indicator of the strength variations in SHGC after exposure to elevated temperatures.

3.4. Uniaxial tensile behaviour

This section presents the uniaxial tensile behaviour of SHGC subjected to elevated temperatures in terms of stress-strain response and tensile properties, including crack number, crack width, first-crack strength, tensile strength, strain capacity, and strain energy, which are summarised in Table 5.

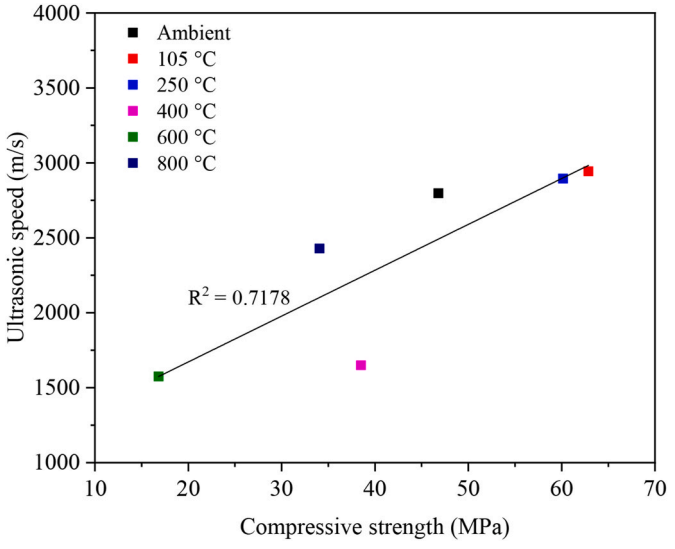

Fig. 10. Relationship between UPV and compressive strength of SHGC exposed to different temperatures.

3.4.1. Stress-strain response

Fig. 11 shows the tensile stress-strain curves of SHGC exposed up to 250 °C since tensile strain-hardening behaviour vanished afterwards as PVA fibres have melted and degraded. SHGC specimens exposed to 400–800 °C failed with one crack when the tensile strengths were reached and thus the corresponding strain to the measured tensile strengths (see Table 5) were not recorded. As observed, the specimens heated up to 250 °C exhibited a similar trend with different magnitudes. Firstly, the tensile stress increased proportionally with the minor strains measured until the limit of proportionality was reached. Then, the curves entered the strain-hardening region with a non-linear behaviour and reduced gradient. In this region, the tensile stress steadily rose with the recorded strain. The stress drops on this part of the curve indicated the formation and propagation of microcracks during tensile loading. During the test, the crack openings were limited as the PVA fibres bridged the cracks, leading to the multiple microcracking behaviour. Eventually, the highest point of tensile stress (i.e., tensile strength) was reached, followed by the failures of specimens.

As seen in Fig. 11, the strain-hardening regions of specimens heated to 105 °C were the longest, followed by that of the ambient ones and then that exposed to 250 °C. The stress-strain curves of unheated specimens exhibited apparent fluctuations in the strain-hardening region due to the steadily developed microcracks. The curves tended to be smoother for the specimens heated to 105 °C, implying that the formed crack openings were smaller and resisted by the fibre-bridging effect (Fig. 12a). Regarding the specimens exposed to 250 °C, the variations of stress-strain curves looked greater than the other groups of specimens with significant reductions in tensile strain capacity because of the melting of PVA fibres.

As cracking behaviour is critical to durability and serviceability of SHGC structural members [84], the crack patterns were captured in the dog-bone central section after the load removal. To clearly demonstrate the crack patterns, the images and their reproductions are displayed in Fig. 13. The cracking behaviour was quantified in terms of crack number and crack width in Table 5. The actual crack numbers and widths might be higher due to the closure of some microcracks after unloading [85]. Multiple microcracks were formed and distributed over the area of interest of specimens exposed up to 250 °C, whilst the specimens failed in one single crack at higher temperatures. At room temperature, the presence of PVA fibres in the geopolymer matrix resulted in saturated crack patterns with a tight average crack width of 29.8 μm. The samples exposed to 105 °C exhibited the highest number of cracks along with a reduced average crack width of 21.7 μm, indicating that the crack-controlling behaviour still retained and was even improved when the specimens were heated to 105 °C. This can be attributed to the slightly reduced tensile strength of PVA fibres under the exposure of 105 °C, which sustained the fibre bridging effect. As seen in Fig. 12a, most PVA fibres were pulled out or bridging at the fracture section of sample at 105 °C with no visible change of appearance, implying that the fibre-matrix bonding and remained tensile strength of fibres were sufficient to avoid fibre rupture at this temperature, resulting in the restrained crack widths and excellent tensile performance [86]. However, the tensile strength of PVA fibres dropped obviously as they started to melt and degraded when the temperature was further increased [87]. Thus, even though multiple cracks were formed in the specimen heated to 250 °C, they were unsaturated as fibres across the crack can easily rupture (Fig. 12b) due to the low tensile strength of fibre and the bond between fibre and geopolymer matrix. In general, the cracking behaviour showed a good agreement with the tensile stress-strain curves above.

Table 5
Key parameters of SHGC exposed to different temperatures in uniaxial direct tensile test.

Temperature (°C)	Average crack number	Average crack width (μm)	Tensile strength (MPa)	First-crack strength (MPa)	Tensile capacity (%)	Tensile energy (kJ/m^3)
Ambient	28 (1)	29.8 (11.6)	3.40 (0.33)	2.38 (0.20)	3.20 (0.57)	97.1 (18.6)
105	34.7 (3.5)	21.7 (11.5)	3.84 (0.14)	2.56 (0.32)	3.22 (0.85)	124.5 (26.2)
250	10 (1)	11.3 (3.1)	4.22 (0.28)	2.82 (0.29)	2.17 (0.17)	89.4 (11.3)
400	1	–	0.32 (0.22)	–	–	–
600	1	–	0.71 (0.22)	–	–	–
800	1	–	0.70 (0.12)	–	–	–

Note: Numbers in parentheses are the standard deviations of corresponding parameters. The average crack number and width were obtained from a previous study [47].

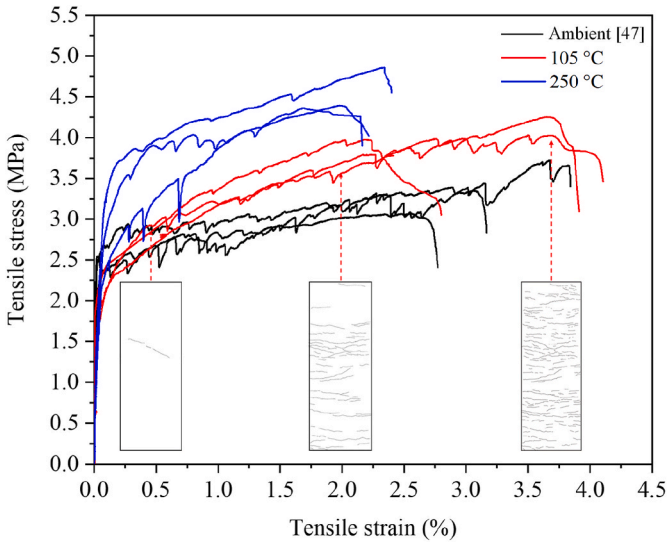

Fig. 11. Tensile stress-strain curve pf SHGC exposed to ambient temperature, 105 °C and 250 °C.

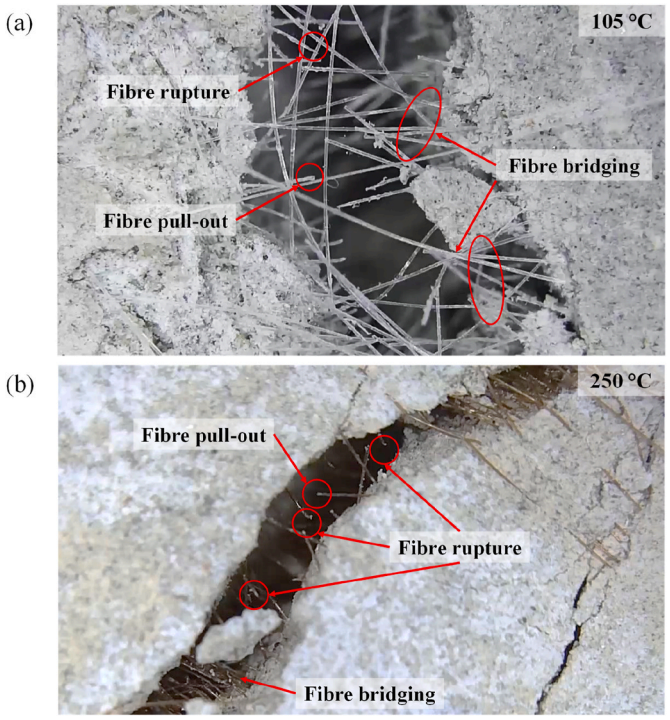

Fig. 12. Fibre status at fracture section of SHGC exposed to (a) 105 °C and (b) 250 °C.

3.4.2. Tensile strength

Fig. 14 presents the first-crack strength of SHGC specimens heated up to 250 °C and tensile strength of all specimens. The initial crack strength and tensile strength of specimens showed a similar tendency that they increased with temperatures below 250 °C as a result of the higher matrix strength caused by further reaction and fibre bridging action. In this temperature range, the first-crack strength and tensile strength were enhanced by 18.4% and 24.2%, respectively, while at higher temperatures, the specimens showed a brittle failure with tensile strength dropped to below 1.0 MPa due to the complete elimination of fibre bridging. However, similar to the compressive behaviour, higher tensile strengths of SHGC were achieved because of the greater strength of geopolymer matrix.

3.4.3. Tensile strain and energy

Fig. 15 displays the measured strain capacity and strain energy of SHGC specimens, indicating a strain-hardening behaviour. These two parameters demonstrated the same tendency as a function of temperature. At room temperature, the samples exhibited an average strain capacity of about 3.20%, followed by a slight increase to 3.22% at 105 °C. Meanwhile, the average strain energy reached its peak value of around 125 kJ/m^3 from 97 kJ/m^3, which is an indicator of a higher strain-hardening degree and energy dissipation capacity. A previous study [45] reported a similar improvement in the tensile properties of heat-curved FA-based SHGC compared to the performance of ambient cured SHGC. Afterwards, the strain capacity and corresponding energy were declined to 2.17% and 89 kJ/m^3 at 250 °C, respectively, which can be mainly ascribed to the thermal impact on embedded PVA fibres in SHGC that deteriorated the post-cracking behaviour of SHGC. The tensile strain capacity of SHGC exposed up to 250 °C was comparable to or higher than that of PVA reinforced SHCC with a mean value of 2.69% at room temperature [88].

3.5. Microstructure evolution

To investigate the damage mechanisms in SHGC subjected to elevated temperatures, the thermal effect on the microstructure of SHGC was studied in terms of phase changes, thermal stability, and morphology and pore structure evolution.

3.5.1. Phase composition

Since this study aims to investigate the overall behaviour of SHGC but not to offer a thorough understanding of gel phases, the phase identification is used as a reference of potential products. The XRD patterns of raw FA and GGBS are shown in Fig. 16a. The crystal peaks in the XRD spectra of FA mainly correspond to quartz (SiO_2) and mullite ($Al_{4.82}Si_{1.18}O_{9.59}$), while the amorphous hump is demonstrated at around 15–30° 2θ. The XRD pattern of raw GGBS showed a board hump, suggesting the presence of glassy phases without sharp peaks that indicate crystallinity.

The XRD patterns of SHGC exposed to elevated temperatures are plotted from 5° to 90° 2θ and given in Fig. 16b and c. Overall, the phase composition of SHGC specimens after heat exposure was relatively

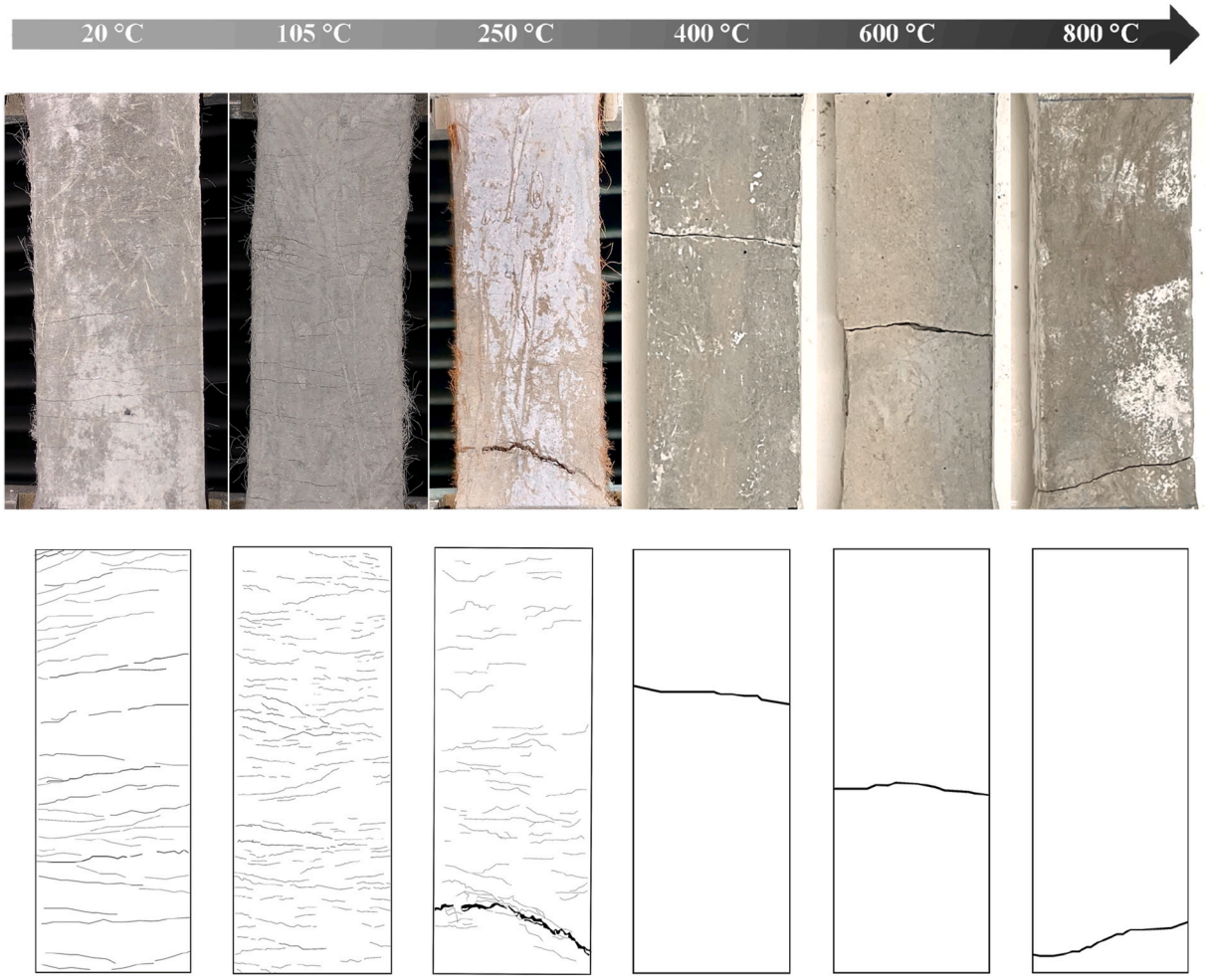

Fig. 13. Real and corresponding reproduced crack patterns in the central gauge area of SHGC exposed to different temperatures.

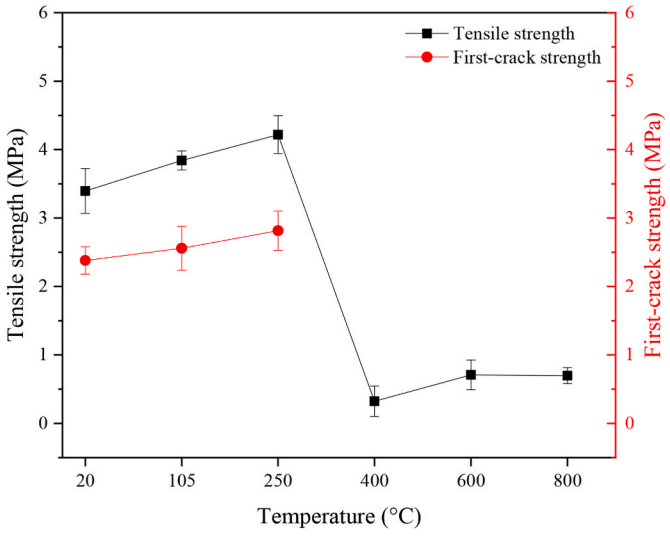

Fig. 14. First-crack strength and tensile strength of SHGC exposed to different temperatures.

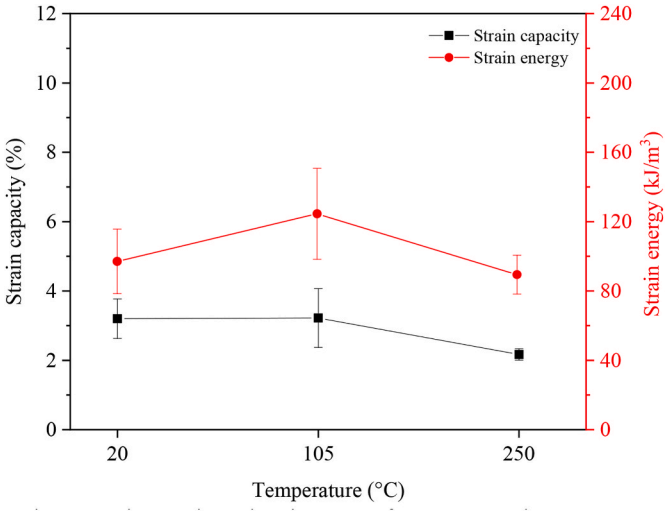

Fig. 15. Strain capacity and strain energy of SHGC exposed up to 250 °C.

stable, with a few new crystallise peaks detected at 105 °C. The crystalline phases including quartz (SiO_2, PDF#01-085-0797) and mullite ($Al_{4.82}Si_{1.18}O_{9.59}$, PDF#96-900-5502) in FA particles at 16.5°, 20.9°, 26.2°, 26.7°, 33.3°, 40.9°, 42.5°, 50.2°, 54.9°, 68.1°, and 81.5° 2θ remained unchanged throughout the heat exposure. Mullite is a stable phase that can retain its room temperature strength at elevated temperatures with a high melting point at 1830 °C, while quartz has a melting point (>1600 °C) higher than the testing range in this study [89, 90]. The amorphous phases defined as the wide and diffusive reflection can be observed in all specimens, indicating the formation of silicate and

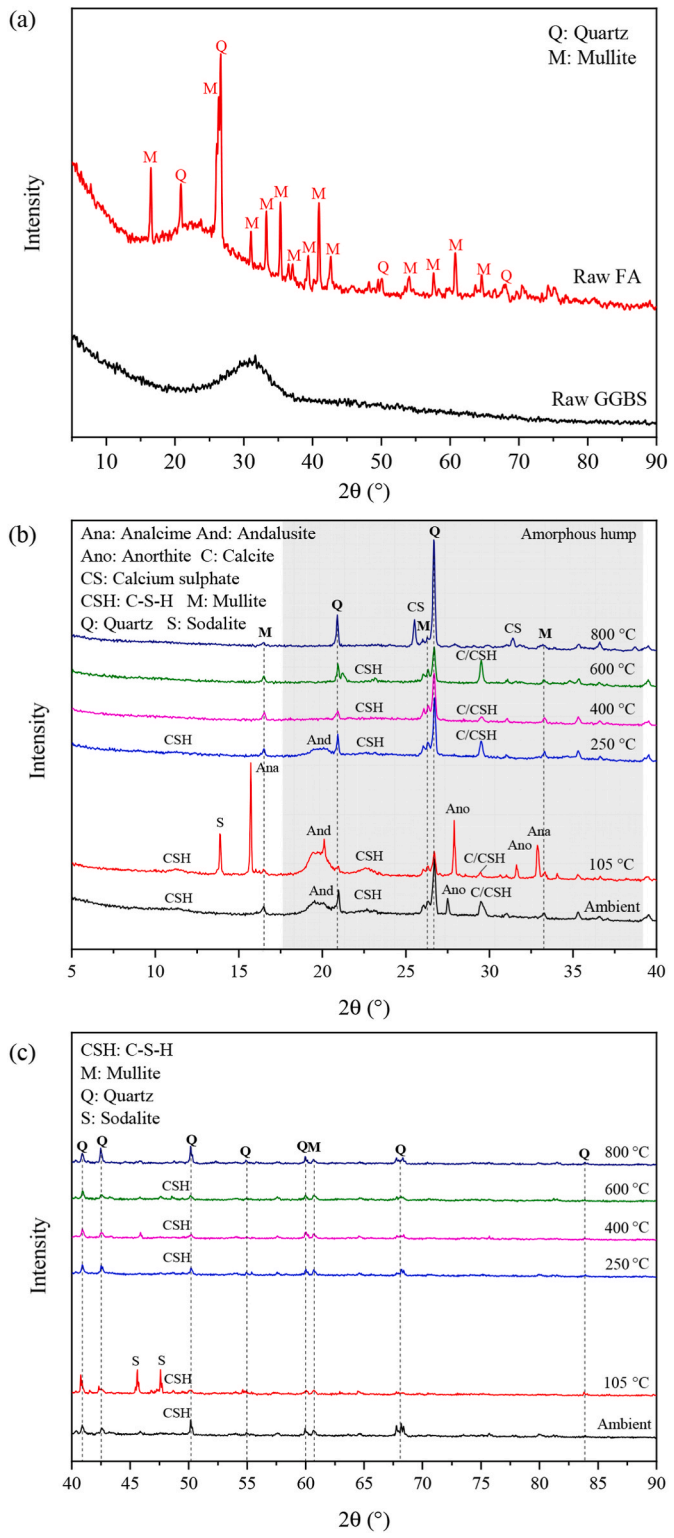

Fig. 16. XRD patterns of (a) raw FA, raw GGBS and SHGC exposed to different temperatures at (b) 5°–45° and (c) 45°–90°.

aluminosilicate gels [91]. At 105 °C, some sodalite ($Na_8(AlSiO_4)_6Cl_2$, PDF#01-088-2088) and analcime ($Na_{0.931}(AlSi_2O_6)(H_2O)$, PDF#01-089-6324) crystalline inclusions were found in the specimens, which are common reaction products presented in FA-based geopolymers subjected to heat curing (below 300 °C) [73,92]. Besides, the detection of anorthites ($(Ca,Na)(Al,Si)_2Si_2O_8$ or $CaAl_2Si_2O_8$, PDF#00-009-0465 or PDF#00-041-1486) indicated the presence of calcium in the reaction at this stage. Up to 250 °C, the crystalline phases of aluminosilicate mineral andalusite (Al_2SiO_4O, PDF#01-089-0887) were also detected. Meanwhile, the diffuse peaks of C–S–H ($CaSO_4 \cdot 2H_2O$, PDF#00-001-0385) at around 11°, 23°, 29°, and 50° 2θ were noticed in the spectra. According to the previous studies [93,94], the peak at 29°–30° 2θ can be related to semi-crystalline C–S–H, calcite, or poorly ordered C–S–H gels. Further, the Si in C–S–H gels could also be substituted with Ai and formed C-A-S-H gels [36,91]. After the exposure to 400 °C, the peaks at 11° 2θ became unnoticeable, whilst the rest of C–S–H was no longer visible when heating to 800 °C. This suggests that C–S–H was barely affected up to the exposure to 250 °C and fully dehydrated at 800 °C [95]. The calcium sulphate ($CaSO_4$, PDF#01-072-0916) phases presented instead in SHGC exposed to 800 °C with no other new crystallises formed.

3.5.2. Thermal analysis

Fig. 17 illustrates the thermal analysis results of SHGC in terms of TGA, DSC, and DTG curves. The total mass reduction of the specimen from ambient temperature to 800 °C was 11.9%. Meanwhile, two distinct peaks can be observed on the DTG curves at around 100 °C and 700 °C. Following the initial rapid drop, the rate of mass loss became stable in the range of 200 °C and 600 °C before another deep peak was shown. The increased rate of mass loss below 200 °C can be associated with the loss of free water and the dehydration of binding phases that took place in this range, which was responsible for 4.6% of mass loss. Then, the steady loss rate and around 5% mass reduction occurred due to the ongoing loss of bound water in the zeolite-like products (gel and crystalline aluminosilicates) along with the decomposition of C–S–H [73]. At the last stage, the mass loss was 2.7% from 600 °C to 800 °C, which was aligned with an increase of loss rate. The peak at 700 °C can be ascribed to the burning coal residuum and the formation of anhydrous calcium sulphate (i.e., anhydrite), as shown in the XRD curve of the specimen exposed to 800 °C [73]. The corresponding DSC curve revealed the presence of only one broad exothermic peak that reflects a heat release process, implying that a complex zeolite-like structure was formed [96,97].

3.5.3. SEM observation

The SEM micrographs with different magnifications are used to assess the thermal effect on the microstructural characteristics of SHGC in relation to fibres, fibre-matrix interfaces, and matrices. Fig. 18 demonstrates the microstructural evolution of the fixed region around PVA fibres in SHGC specimens. Unlike conventional cementitious materials, the geopolymer matrix shows a relatively porous structure, especially when it was heated to 800 °C [98]. The fibres did not undergo a significant alteration after exposure to 105 °C (Fig. 18b), after which they melted and shrank at 250 °C. At 400 °C, the fibres experienced

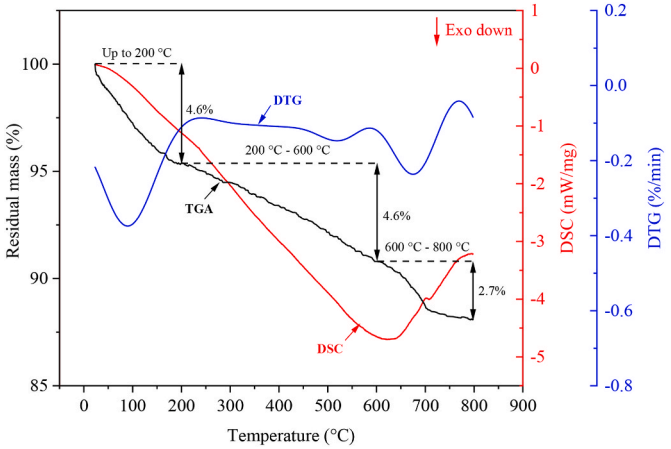

Fig. 17. TGA, DSC and DSC curves of SHGC exposed to elevated temperatures.

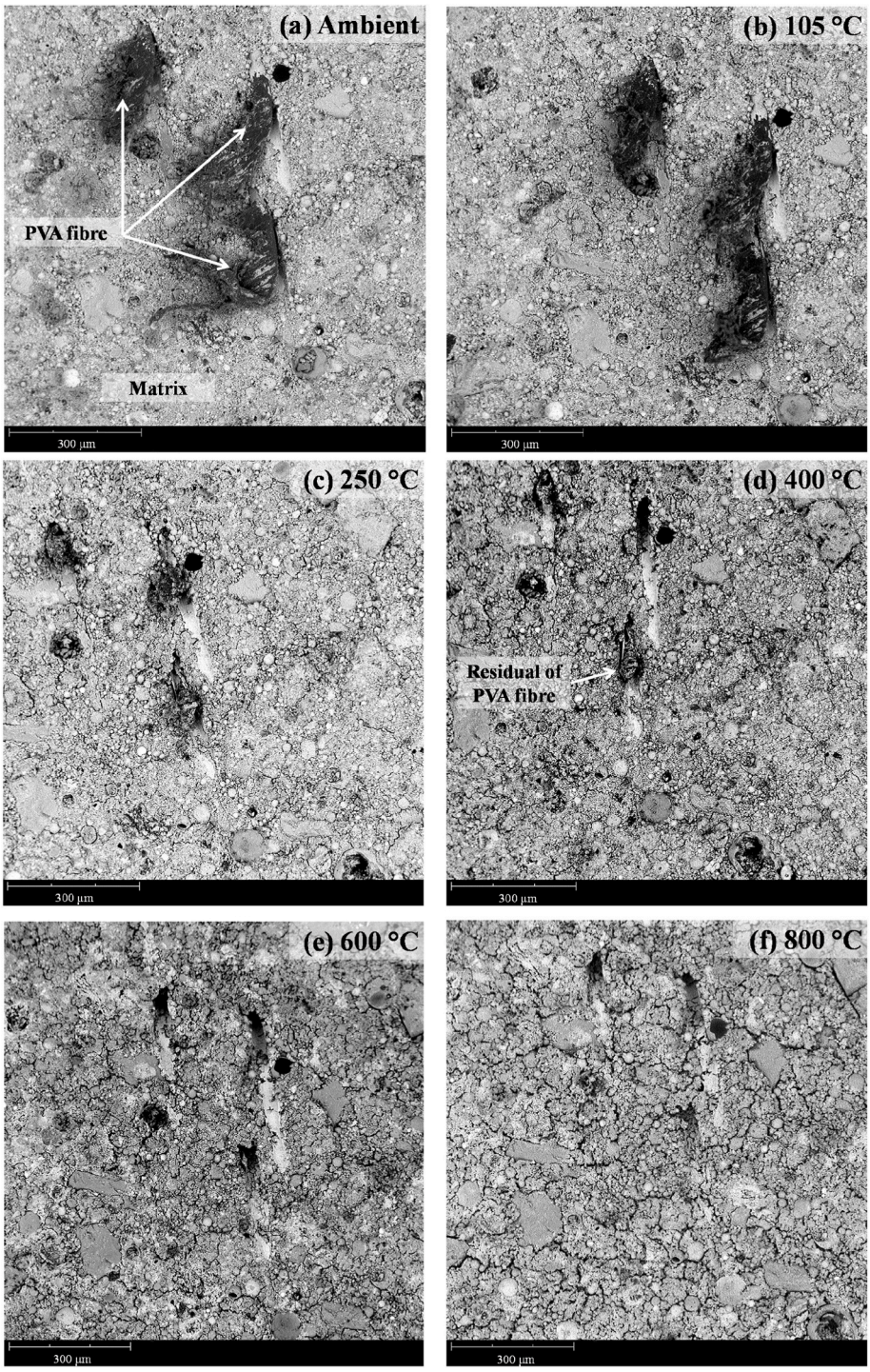

Fig. 18. SEM images of a fixed region around PVA fibres in SHGC at elevated temperatures.

degradation with minimal residuals left, generating interconnected empty channels in the matrix as observed in Fig. 18d–f. Fig. 19 shows closer views of fibre-matrix interfaces in SHGC exposed up to 250 °C. The generation of microcracks around fibres and pronounced damage of fibre surface can be seen at this scale. The visible fibre path and reaction products attached to fibres (Fig. 19b) indicated the high level of fibre-matrix interaction due to the inherent chemical bond of hydrophilic PVA fibres [99]. As the temperature increased, the interfacial bonding was weakened, as demonstrated in the reduced matrix fragments clung on the fibre surfaces.

Fig. 20 displays the geopolymer matrix characteristics at a larger scale which dominate the mechanical behaviour of SHGC after the loss of fibres. Overall, all matrices consisted of gels that were continuous, dense, and bulky in structure, together with various quantities of pores and cracks. The wide exothermic peak in DSC curve along with the amorphous humps and calcium crystallise peaks in the XRD spectra suggested the possible presence of aluminosilicate gels such as N-A-S-H, C–S–H, and C-A-S-H. The microstructure of the unheated specimen was composed of a large portion of binding gels and inserted unreacted particles (Fig. 20a). Conforming to the XRD patterns, mullite crystals can be observed as the needle-like particles attached to the spherical FA particles. Further, unreacted FA particles appeared in the cavities at

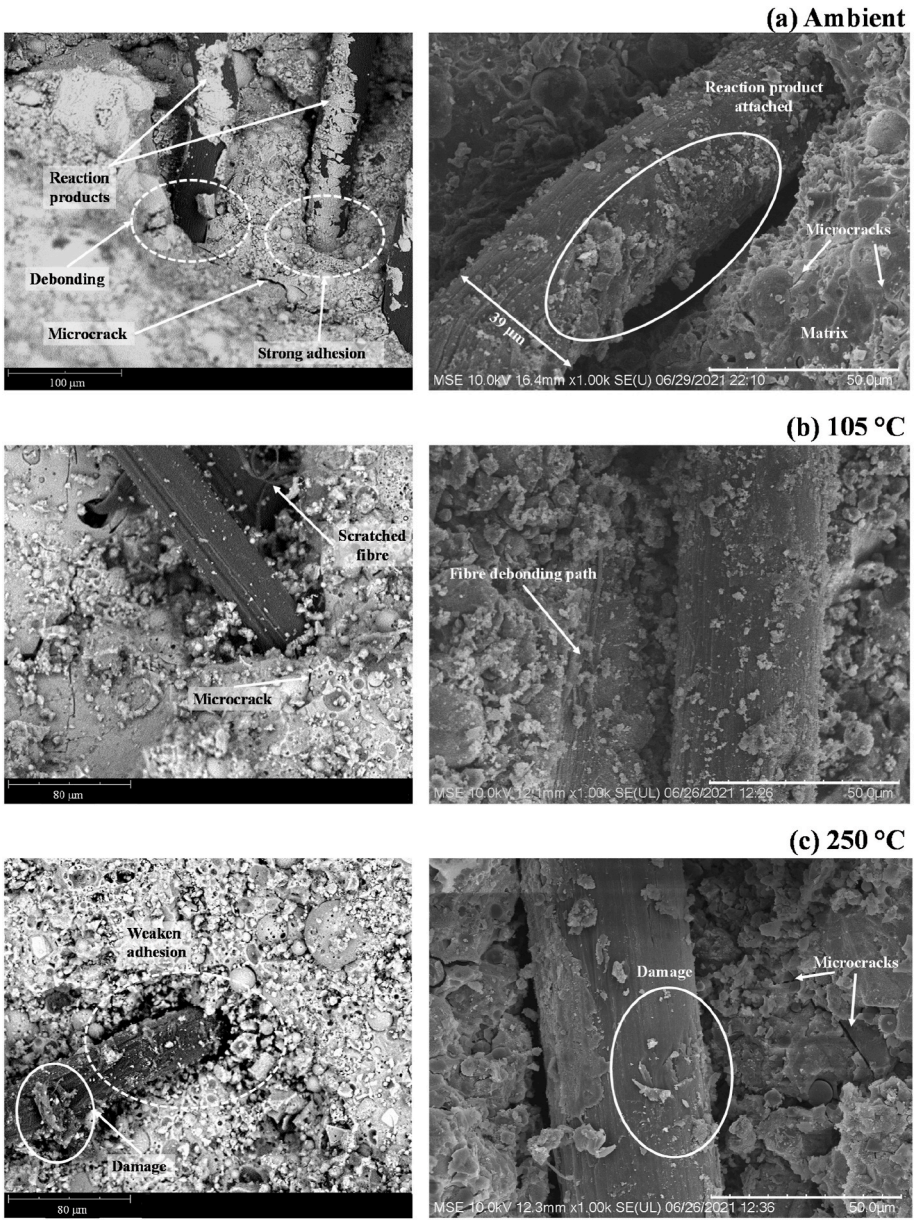

Fig. 19. SEM images of fibre-matrix interfaces in SHGC exposed to (a) ambient temperature, (b) 105 °C, and (c) 250 °C.

both room and higher temperatures, implying that a great amount of FA remained unreacted or partially reacted at the elevated temperatures. After the exposure of 400 °C (Fig. 20b), excessive larger microcracks were formed and connected due to fibre evaporation. It is also displayed that microcracks could propagate through the comparatively weak route, e.g., the voids around the unreacted particles. Meanwhile, cavities distributed on gels can be observed, which may be attributed to the fractured surface passing through detached unreacted FA particles that did not shrink as opposed to the gel base. The shrinkage in gels might also result in the development of more microcracks [18]. After this, Fig. 20c shows the sign of sintering at 600 °C with an increased degree of this effect at 800 °C (Fig. 20d), leading to a more homogeneous and denser microstructure. Simultaneously, enlarged pores were formed as the viscous flow of gel closed smaller pores.

3.5.4. Pore structure

The pore structure of SHGC at elevated temperatures was characterised using MIP, the results of which are presented in Table 6, demonstrating some important features of pore structure at different temperatures. First, the total porosity of SHGC reduced gradually from 24.6% to 20.8% as the temperature rose from ambient to 250 °C, while the pore size became larger as indicated in the average pore diameters (d_a). Second, the porosity was almost double when the temperature was increased to 400 °C with a reduced d_a of 20.9 nm, followed by a decline of porosity at 600 °C. Finally, the porosity reached the highest value of 45.9%, accompanied by the largest d_a of 166.6 nm at 800 °C.

To better describe the effect of elevated temperature on pore size of SHGC, the pores are divided into four groups in terms of diameters: Group I (<100 nm), Group II (100 nm–1000 nm), Group III (1000 nm–10000 nm), and Group IV (>10000 nm) [100]. The derivative PSD curves are plotted in Fig. 21, together with the corresponding critical pore diameters (d_c) derived from the first peaks appeared on the graph. In this study, the porosity and PSD were mainly influenced by three factors, namely the inherent voids in matrices, the microcracks developed, and the empty channels formed by degraded PVA fibres.

Owing to the promoted formation of cross-linked binder gels that led to continuous refinement of pores, the pore fraction in Group I dropped, resulting in the reduction of overall porosity at 105 °C and 250 °C [36].

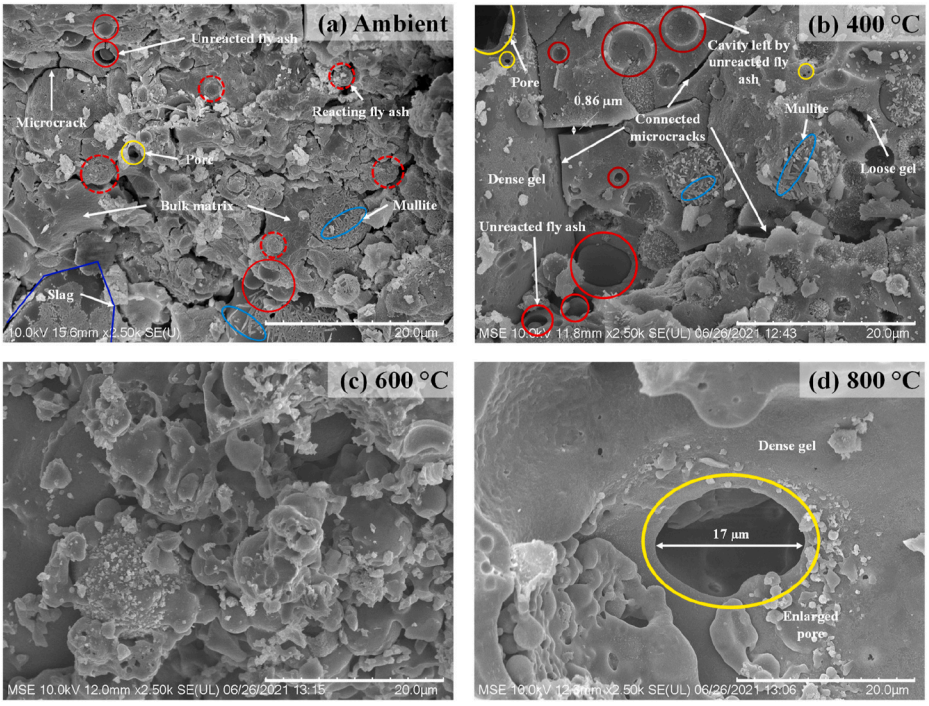

Fig. 20. SEM images of matrix exposed to (a) ambient temperature, (b) 400 °C, (c) 600 °C, and (d) 800 °C.

Table 6
Pore parameters of SHGC exposed to different temperatures obtained from MIP.

Temperature (°C)	Porosity (%)	Critical pore diameter, d_c (nm)	Average pore diameter, d_a (nm)
Ambient	24.6	5.2	12.9
105	22.6	9.1	17.5
250	20.8	11.1	24.0
400	40.5	11.1	20.9
600	26.2	12.3	52.2
800	45.4	3230.0	166.6

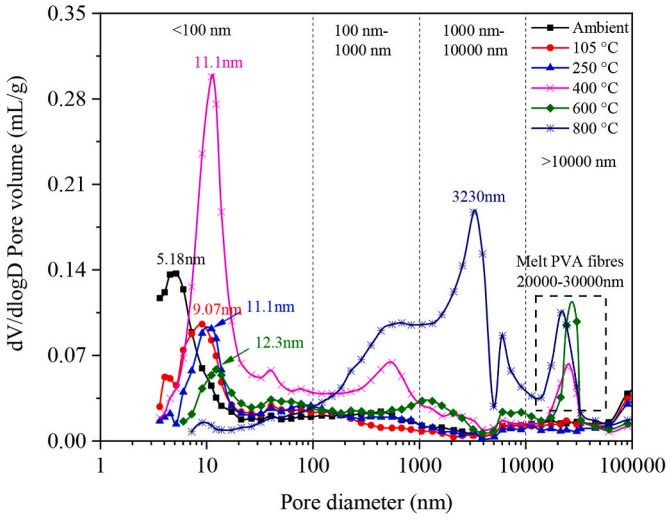

Fig. 21. Pore size distribution of SHGC exposed to elevated temperatures.

As the exposure temperature increased, the vapour induced by melted fibres and internal water rapidly migrated, leading to the microcrack formations and the increase of measured pore volumes. This would also potentially open up some of the closed pores that in turn increased the porosity within the samples [17], resulting in a rapid grow of Group II pores when the temperature reached 400 °C. Meanwhile, a great number of small pores in Group I were generated, leading to a smaller d_a. Additionally, a new peak was formed clearly at around 25000 nm in Group IV, which corresponds to the channels left by the melted PVA fibres with a diameter of 40000 nm and residuals. This peak became more intense at 600 °C, implying more macropores were formed in the specimens and led to the increase of d_a. However, when exposed to 600 °C, the porosity of SHGC was significantly decreased from 40.5% to 26.2%, indicating the microstructure was densified to a certain extent, i.e., crack healing. Compared to the other five derivative curves, the curve of samples heated to 800 °C shifted to the right with a d_c of 3230 nm with many pores fell into Group III. This can be ascribed to the microcracks induced by the dehydration of C–S–H, along with the collapse of smaller pores that formed extensive larger voids due to the sintering effect. The evidence of sintering in the pore structure at 800 °C can also be observed in the much denser gel, i.e., reduction in Group I [18].

4. Discussion

This section further analyses the results above to understand the mechanisms of relevant changes in SHGC exposed to elevated temperatures. Overall, the thermal effect on the mechanical properties of SHGC can be reflected in its microstructural evolution at elevated temperatures. The mechanisms for mechanical enhancement or deterioration include dehydration, fibre bridging, fibre degradation and evaporation, physicochemical changes, and sintering. Fig. 22 shows the relationship between compressive strength and major microstructural changes occurred in SHGC. Based on the variations in the macroscopic properties of SHGC, the analysis can be divided into four stages by means of temperature range, including Stage I (20–105 °C), Stage II (105–250 °C), Stage III (250–600 °C), and Stage IV (600–800 °C).

During Stage I, the compressive strength of SHGC increased mainly due to the continuous geopolymerisation of matrix and PVA fibre action that restricted the growth of cracks initiated under loading. The former reason is implicated by the new formation of crystalline peaks in the XRD pattern, along with the reduction of pores with diameters <100 nm.

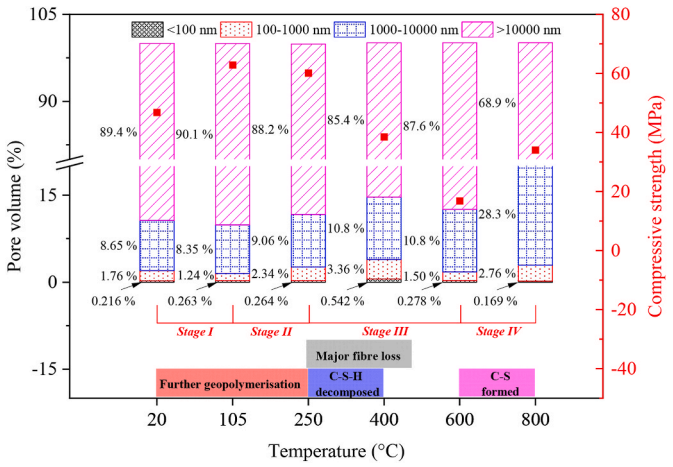

Fig. 22. Relationship between microstructure evolution and compressive strength of SHGC at elevated temperatures.

These pores can be assigned to gel pores and medium capillary pores that were refined because of the newly formed reaction products [31]. Meanwhile, the apparently attached matrix fragment on fibres in the SEM image indicated the strong fibre-matrix bond, suggesting that extra energy absorption was provided by PVA fibres in SHGC. Although few dehydration damages induced by escaping water occurred at Stages I and II, the densified microstructure as indicated by reduced porosity dominated the strength gain. This also explains the enhanced first-crack strength of SHGC in the uniaxial tensile test since the first crack was initiated as the tensile capacity of geopolymer matrix was exceeded.

Before and during Stages I and II, the tensile behaviour of SHGC is directly associated with the fibre status at cross-sections when crack openings increased. As the crack kept propagating and reached the PVA fibres, fibres underwent different statuses, i.e., bridging, rupture or pull out, depending on the fibre-matrix interaction that influences macroscopic properties. Fibres can be completely pulled out or ruptured with an excessively weak or strong interfacial bond, respectively. A bridging action can be triggered with a moderate interfacial bond that elongates the fibre without rupturing it, which is favourable to the strain-hardening and crack controlling behaviour. From the SEM observation of the unheated SHGC sample, the surface roughness of PVA fibres was the highest with more geopolymer products attached, indicating the strongest bond behaviour among all samples. Thus, it can be suggested that the fibre-matrix bond at ambient temperature was sufficient to deform fibres, whilst larger quantities of fibres bridged the opening cracks as reflected by its satisfactory tensile performance. This has been verified by a previous study [47] regarding the robust strain-hardening and multiple cracking behaviour along with high strain-hardening indices and SEM images showing pronounced matrix fragments attached that implies the superior bond between fibre and geopolymer matrix.

Moreover, after Stage I, when the temperature exceeded 105 °C, the fibre-matrix bond was weakened as the fragments attached to PVA fibres were reduced. Nevertheless, the bond was still adequate to elongate fibres, which is implied by the captured fibre footprint. Hence, the SHGC specimens exposed to 105 °C exhibited the best tensile strain capacity, strain energy, and crack-controlled behaviour since the fibres in these specimens were less likely to rupture. The enhanced tensile performance was previously reported in sole FA-based SHGC with heat curing (60 °C), suggesting that the mechanical properties of SHGC with 20 wt% GGBS in this study had a similar response at elevated temperatures [45]. Then, at Stage II, the high temperature reduced the tensile strength of fibres, as revealed by the visible damage on PVA fibre in the SEM images. As a result, fibres were easily ruptured upon tension, leading to the halve of strain capacity and strain energy of SHGC at 250 °C as the tensile strength of fibres was inadequate to resist the fibre-matrix bond at this stage even though it was weakened.

The PVA fibre employed has a melting point of 248 °C with more than 90% weight loss observed below 475 °C. Therefore, at Stage III, the evaporation of fibres induced pressure build-up in the dense pore structure and resulted in large numbers of microcracks. Besides, as indicated by TGA, the dehydration in gel products took place, which could facilitate the microcrack formation by shrinkage and internal stresses [73,101]. Therefore, there is an obvious increase in porosity and transformation of larger pore sizes (>1000 nm) at 400 °C. Meanwhile, the C–S–H peak in the XRD pattern disappeared, meaning that C–S–H decomposed during Stage III. All these have promoted the considerable strength loss at this stage, and hence the strength reached its minimum value at 600 °C. Moreover, in this evolution stage, overall porosity showed a significant drop with reduced pore volume in the range of 1000–10000 nm, implying the microcrack healing performance in the system, which was confirmed by the smoother flowing microstructure in the micrograph.

Finally, at Stage IV, the compressive strength of SHGC was enhanced with a notable change in pore structure features. The sintering effect played a vital role in collapsing the smallest pores (<100 nm) due to the viscous flow of gels and partial FA particles, leading to the densification of gel structure that is responsible for the strength gain. Nevertheless, the strength at 800 °C was still lower than that at ambient temperature, which may be attributed to the macro-cracks induced by shrinkage of pores and uneven stresses over the specimens [74]. Ranging from 400 °C to 800 °C, the strain-hardening behaviour was invisible with a minimal retained tensile strength that followed the same changing trend as compressive behaviour due to the fibre loss.

5. Conclusions

In this study, a series of tests including uniaxial compression, uniaxial tension, UPV, TGA, DSC, XRD, SEM, and MIP were conducted to investigate the engineering properties and microstructural evolution of fly ash-slag based strain hardening geopolymer composite (SHGC) cured at ambient temperature exposed to elevated temperatures, i.e., ambient, 105 °C, 250 °C, 400 °C, 600 °C, and 800 °C. Based on the experimental results, the major conclusions can be drawn as follows:

- The change in phase composition and internal structure of geopolymer matrix, along with the fibre bridging action affected the mechanical properties of SHGC at elevated temperatures. In detail: (1) From the room temperature to 250 °C, the mechanical properties of SHGC were mainly dependent on the ongoing geopolymerisation and the fibre bridging action. The densification of pore structure and tight bonding between fibre and matrix effectively enhanced the compressive strength of SHGC to 134.3% of the original at 105 °C. (2) At 400 °C and 600 °C, the extensive formation of microcracks and decomposition of strength-given phases decreased the compressive strength of SHGC to around one-third of the initial strength. (3) The sintering effect at 800 °C significantly reduced the size of pores with diameters <100 nm and densified the microstructure. Hence, the regain of compressive strength of SHGC presented because of the homogeneous microstructure. In addition, no spalling was observed in all SHGC specimens due to the inherent porous structure of geopolymer matrix.
- The tensile strength of SHGC before the loss of fibre is highly associated with the matrix strength, whilst strain-hardening degree and multiple cracking behaviour depend on the temperature-induced changes in PVA fibre which also affect fibre-matrix bonding. SHGC exposed to 105 °C yielded the best tensile performance among all samples, which achieved a tensile strain capacity of 3.22%. This was achieved by the moderate fibre-matrix bonding that was adequate to deform fibres without rupturing them, resulting in the fibre bridging

mechanism that controlled crack growths and promoted strain-hardening degree.

- SHGC is a multiphase composite material mainly consisting of amorphous products, unreacted or partially reacted fly ash and slag particles, crystalline phases and pores, as well as the inserted PVA fibres. The characteristics of these phases were differently influenced by the thermal exposure. Overall, no significant change can be observed in the crystalline phases in fly ash particles, whilst unreacted particles still presented in SHGC exposed to high temperatures. The calcium compounds remained stable up to 250 °C and were susceptible to decomposition and crystallisation afterwards. Moreover, the crystalline phases (e.g., sodalite and analcime) can be found at 105 °C, while calcium sulphates appeared at 800 °C without other new crystalline formed.
- Regarding the evolution of pore structure of SHGC, the pore size distribution gradually shifted to larger voids at 400 °C and 600 °C, which can be ascribed to the dehydration damages that induced microcracks, the fibre-induced channels that introduced macropores, and the sintering that reduced the amount of gel pores and increased the number of larger pores. Instead of overall porosity, pore size distribution was found to be more associated with strength of SHGC, where the reduced volume fraction of small pores is highly correlated with the strength gain.

Declaration of competing interest

The authors declare that they have no known competing financial interests or personal relationships that could have appeared to influence the work reported in this paper.

Acknowledgements

The authors gratefully acknowledge the financial support from the Engineering and Physical Sciences Research Council (EPSRC) under Grant No. EP/R041504/1 and the Royal Society under Award No. IEC \NSFC\191417.

References

[1] J. Zhao, J.J. Zheng, G.F. Peng, P.S. Sun, Spalling and cracking modelling of high-performance concrete exposed to elevated temperatures, Mag. Concr. Res. 69 (2017) 1276–1287, https://doi.org/10.1680/jmacr.16.00139.
[2] V. Kodur, Properties of concrete at elevated temperatures, 2014, ISRN Civ. Eng. (2014), 468510, https://doi.org/10.1155/2014/468510.
[3] T.R. Board, of Sciences Engineering, Medicine, Design Fires in Road Tunnels, The National Academies Press, Washington, DC, 2011, https://doi.org/10.17226/14562.
[4] C. Shi, A.F. Jiménez, A. Palomo, New cements for the 21st century: the pursuit of an alternative to Portland cement, Cement Concr. Res. 41 (2011) 750–763, https://doi.org/10.1016/J.CEMCONRES.2011.03.016.
[5] J.L. Provis, Alkali-activated materials, Cement Concr. Res. 114 (2018) 40–48, https://doi.org/10.1016/J.CEMCONRES.2017.02.009.
[6] J.L. Provis, 4 - activating solution chemistry for geopolymers, in: J.L. Provis, J.S. J. van Deventer (Eds.), Geopolymers, Woodhead Publishing, 2009, pp. 50–71, https://doi.org/10.1533/9781845696382.1.50.
[7] T. Matsunaga, J.K. Kim, S. Hardcastle, P.K. Rohatgi, Crystallinity and selected properties of fly ash particles, Mater. Sci. Eng. 325 (2002) 333–343, https://doi.org/10.1016/S0921-5093(01)01466-6.
[8] T. Phoo-Ngernkham, P. Chindaprasirt, V. Sata, T. Sinsiri, High calcium fly ash geopolymer containing diatomite as additive, Indian J. Eng. Mater. Sci. 20 (2013) 310–318.
[9] A. Palomo, M.W. Grutzeck, M.T. Blanco, Alkali-activated fly ashes: a cement for the future, Cement Concr. Res. 29 (1999) 1323–1329, https://doi.org/10.1016/S0008-8846(98)00243-9.
[10] X.Y. Zhuang, L. Chen, S. Komarneni, C.H. Zhou, D.S. Tong, H.M. Yang, W.H. Yu, H. Wang, Fly ash-based geopolymer: clean production, properties and applications, J. Clean. Prod. 125 (2016) 253–267, https://doi.org/10.1016/j.jclepro.2016.03.019.
[11] A. Fernandez-Jimenez, I. García-Lodeiro, A. Palomo, Durability of alkali-activated fly ash cementitious materials, J. Mater. Sci. 429 (42) (2006) 3055–3065, https://doi.org/10.1007/S10853-006-0584-8, 2006.
[12] P. Duxson, J.L. Provis, G.C. Lukey, J.S.J. van Deventer, The role of inorganic polymer technology in the development of "green concrete, Cement Concr. Res. 37 (2007) 1590–1597, https://doi.org/10.1016/j.cemconres.2007.08.018.
[13] X. Guo, H. Shi, W.A. Dick, Compressive strength and microstructural characteristics of class C fly ash geopolymer, Cem. Concr. Compos. 32 (2010) 142–147, https://doi.org/10.1016/J.CEMCONCOMP.2009.11.003.
[14] A. Fernández-Jiménez, J.Y. Pastor, A. Martín, A. Palomo, High-temperature resistance in alkali-activated cement, J. Am. Ceram. Soc. 93 (2010) 3411–3417, https://doi.org/10.1111/j.1551-2916.2010.03887.x.
[15] T. Bakharev, Thermal behaviour of geopolymers prepared using class F fly ash and elevated temperature curing, Cement Concr. Res. 36 (2006) 1134–1147, https://doi.org/10.1016/J.CEMCONRES.2006.03.022.
[16] W.D.A. Rickard, J. Temuujin, A. Van Riessen, Thermal analysis of geopolymer pastes synthesised from five fly ashes of variable composition, J. Non-Cryst. Solids 358 (2012) 1830–1839, https://doi.org/10.1016/j.jnoncrysol.2012.05.032.
[17] M. Lahoti, K.K. Wong, K.H. Tan, E.H. Yang, Effect of alkali cation type on strength endurance of fly ash geopolymers subject to high temperature exposure, Mater. Des. 154 (2018) 8–19, https://doi.org/10.1016/J.MATDES.2018.05.023.
[18] W.D.A. Rickard, C.S. Kealley, A. Van Riessen, Thermally induced microstructural changes in fly ash geopolymers: experimental results and proposed model, J. Am. Ceram. Soc. 98 (2015) 929–939, https://doi.org/10.1111/jace.13370.
[19] F. Fan, Z. Liu, G. Xu, H. Peng, C.S. Cai, Mechanical and thermal properties of fly ash based geopolymers, Construct. Build. Mater. 160 (2018) 66–81, https://doi.org/10.1016/j.conbuildmat.2017.11.023.
[20] D.L.Y. Kong, J.G. Sanjayan, Damage behavior of geopolymer composites exposed to elevated temperatures, Cem. Concr. Compos. 30 (2008) 986–991, https://doi.org/10.1016/j.cemconcomp.2008.08.001.
[21] D.L.Y. Kong, J.G. Sanjayan, K. Sagoe-Crentsil, Comparative performance of geopolymers made with metakaolin and fly ash after exposure to elevated temperatures, Cement Concr. Res. 37 (2007) 1583–1589, https://doi.org/10.1016/J.CEMCONRES.2007.08.021.
[22] C. Kuenzel, L.J. Vandeperre, S. Donatello, A.R. Boccaccini, C. Cheeseman, Ambient temperature drying shrinkage and cracking in metakaolin-based geopolymers, J. Am. Ceram. Soc. 95 (2012) 3270–3277, https://doi.org/10.1111/j.1551-2916.2012.05380.x.
[23] T. Bakharev, Geopolymeric materials prepared using Class F fly ash and elevated temperature curing, Cement Concr. Res. 35 (2005) 1224–1232, https://doi.org/10.1016/J.CEMCONRES.2004.06.031.
[24] K. Somna, C. Jaturapitakkul, P. Kajitvichyanukul, P. Chindaprasirt, NaOH-activated ground fly ash geopolymer cured at ambient temperature, Fuel 90 (2011) 2118–2124, https://doi.org/10.1016/j.fuel.2011.01.018.
[25] Y. Fan, S. Yin, Z. Wen, J. Zhong, Activation of fly ash and its effects on cement properties, Cement Concr. Res. 29 (1999) 467–472, https://doi.org/10.1016/S0008-8846(98)00178-1.
[26] S. Saha, C. Rajasekaran, Enhancement of the properties of fly ash based geopolymer paste by incorporating ground granulated blast furnace slag, Construct. Build. Mater. 146 (2017) 615–620, https://doi.org/10.1016/J.CONBUILDMAT.2017.04.139.
[27] S. Puligilla, P. Mondal, Role of slag in microstructural development and hardening of fly ash-slag geopolymer, Cement Concr. Res. 43 (2013) 70–80, https://doi.org/10.1016/J.CEMCONRES.2012.10.004.
[28] S. Kumar, R. Kumar, S.P. Mehrotra, Influence of granulated blast furnace slag on the reaction, structure and properties of fly ash based geopolymer, J. Mater. Sci. 45 (2010) 607–615, https://doi.org/10.1007/s10853-009-3934-5.
[29] F. Puertas, S. Martínez-Ramírez, S. Alonso, T. Vázquez, Alkali-activated fly ash/slag cements: strength behaviour and hydration products, Cement Concr. Res. 30 (2000) 1625–1632, https://doi.org/10.1016/S0008-8846(00)00298-2.
[30] N.K. Lee, H.K. Lee, Reactivity and reaction products of alkali-activated, fly ash/slag paste, Construct. Build. Mater. 81 (2015) 303–312, https://doi.org/10.1016/J.CONBUILDMAT.2015.02.022.
[31] G. Fang, M. Zhang, Multiscale micromechanical analysis of alkali-activated fly ash-slag paste, Cement Concr. Res. 135 (2020), 106141, https://doi.org/10.1016/j.cemconres.2020.106141.
[32] G. Fang, Q. Wang, M. Zhang, In-situ X-ray tomographic imaging of microstructure evolution of fly ash and slag particles in alkali-activated fly ash-slag paste, Compos. B Eng. 224 (2021), 109221, https://doi.org/10.1016/j.compositesb.2021.109221.
[33] G. Fang, Q. Wang, M. Zhang, Micromechanical analysis of interfacial transition zone in alkali-activated fly ash-slag concrete, Cem. Concr. Compos. 119 (2021), 103990, https://doi.org/10.1016/j.cemconcomp.2021.103990.
[34] I. Hager, M. Sitarz, K. Mróz, Fly-ash based geopolymer mortar for high-temperature application – effect of slag addition, J. Clean. Prod. 316 (2021), 128168, https://doi.org/10.1016/J.JCLEPRO.2021.128168.
[35] Z. Pan, Z. Tao, Y.F. Cao, R. Wuhrer, T. Murphy, Compressive strength and microstructure of alkali-activated fly ash/slag binders at high temperature, Cem. Concr. Compos. 86 (2018) 9–18, https://doi.org/10.1016/J.CEMCONCOMP.2017.09.011.
[36] S.M. Park, J.G. Jang, N.K. Lee, H.K. Lee, Physicochemical properties of binder gel in alkali-activated fly ash/slag exposed to high temperatures, Cement Concr. Res. 89 (2016) 72–79, https://doi.org/10.1016/j.cemconres.2016.08.004.
[37] N.K. Lee, K.T. Koh, G.H. An, G.S. Ryu, Influence of binder composition on the gel structure in alkali activated fly ash/slag pastes exposed to elevated temperatures, Ceram. Int. 43 (2017) 2471–2480, https://doi.org/10.1016/j.ceramint.2016.11.042.
[38] S. Çelikten, M. Sarıdemir, İ. Özgür Deneme, Mechanical and microstructural properties of alkali-activated slag and slag + fly ash mortars exposed to high temperature, Construct. Build. Mater. 217 (2019) 50–61, https://doi.org/10.1016/J.CONBUILDMAT.2019.05.055.

[39] M. Guerrieri, J.G. Sanjayan, Behavior of combined fly ash/slag-based geopolymers when exposed to high temperatures, Fire Mater. 34 (2010) 163–175, https://doi.org/10.1002/fam.1014.
[40] N. Ranjbar, M. Zhang, Fiber-reinforced geopolymer composites: a review, Cem. Concr. Compos. (2020), https://doi.org/10.1016/j.cemconcomp.2019.103498.
[41] F.U.A. Shaikh, Deflection hardening behaviour of short fibre reinforced fly ash based geopolymer composites, Mater. Des. 50 (2013) 674–682, https://doi.org/10.1016/j.matdes.2013.03.063.
[42] V.C. Li, From Micromechanics to Structural Engineering - the Design of Cementitous Composites for Civil Engineering Applications, 1993. http://deepblue.lib.umich.edu/handle/2027.42/84735. (Accessed 25 February 2021).
[43] V.C. Li, C.K.Y. Leung, Steady-state and multiple cracking of short random fiber composites, J. Eng. Mech. 118 (1992) 2246–2264.
[44] V.C. Li, On engineered cementitious composites (ECC): a review of the material and its applications, J. Adv. Concr. Technol. 1 (2003) 215–230, https://doi.org/10.3151/jact.1.215.
[45] M. Ohno, V.C. Li, A feasibility study of strain hardening fiber reinforced fly ash-based geopolymer composites, Construct. Build. Mater. 57 (2014) 163–168, https://doi.org/10.1016/j.conbuildmat.2014.02.005.
[46] B. Nematollahi, J. Sanjayan, F.U.A. Shaikh, Matrix design of strain hardening fiber reinforced engineered geopolymer composite, Compos. B Eng. 89 (2016) 253–265, https://doi.org/10.1016/j.compositesb.2015.11.039.
[47] H. Zhong, M. Zhang, Effect of recycled tyre polymer fibre on engineering properties of sustainable strain hardening geopolymer composites, Cem. Concr. Compos. 122 (2021), 104167, https://doi.org/10.1016/j.cemconcomp.2021.104167.
[48] B.Y. Lee, C.G. Cho, H.J. Lim, J.K. Song, K.H. Yang, V.C. Li, Strain hardening fiber reinforced alkali-activated mortar - a feasibility study, Construct. Build. Mater. 37 (2012) 15–20, https://doi.org/10.1016/j.conbuildmat.2012.06.007.
[49] B. Nematollahi, J. Sanjayan, J. Qiu, E.H. Yang, Micromechanics-based investigation of a sustainable ambient temperature cured one-part strain hardening geopolymer composite, Construct. Build. Mater. 131 (2017) 552–563, https://doi.org/10.1016/j.conbuildmat.2016.11.117.
[50] Y. Ling, K. Wang, W. Li, G. Shi, P. Lu, Effect of slag on the mechanical properties and bond strength of fly ash-based engineered geopolymer composites, Compos. B Eng. 164 (2019) 747–757, https://doi.org/10.1016/j.compositesb.2019.01.092.
[51] M. Şahmaran, E. Özbay, H.E. Yücel, M. Lachemi, V.C. Li, Effect of fly ash and PVA fiber on microstructural damage and residual properties of engineered cementitious composites exposed to high temperatures, J. Mater. Civ. Eng. 23 (2011) 1735–1745, https://doi.org/10.1061/(asce)mt.1943-5533.0000335.
[52] M.L. Mustafa Sahmaran and Victor C. Li, Assessing Mechanical Properties and Microstructure of Fire-Damaged Engineered Cementitious Composites, ACI Mater. J. 107 (n.d.). https://doi.org/10.14359/51663759.
[53] G. Fares, M.I. Khan, S. Mourad, W. Abbass, Evaluation of PVA and PBI-based engineered-cementitious composites under different environments, Construct. Build. Mater. 85 (2015) 109–118, https://doi.org/10.1016/J.CONBUILDMAT.2015.03.080.
[54] P. Behera, V. Baheti, J. Militky, P. Louda, Elevated temperature properties of basalt microfibril filled geopolymer composites, Construct. Build. Mater. 163 (2018) 850–860, https://doi.org/10.1016/j.conbuildmat.2017.12.152.
[55] A. Celik, K. Yilmaz, O. Canpolat, M.M. Al-mashhadani, Y. Aygörmez, M. Uysal, High-temperature behavior and mechanical characteristics of boron waste additive metakaolin based geopolymer composites reinforced with synthetic fibers, Construct. Build. Mater. 187 (2018) 1190–1203, https://doi.org/10.1016/j.conbuildmat.2018.08.062.
[56] Y. Aygörmez, O. Canpolat, M.M. Al-mashhadani, M. Uysal, Elevated temperature, freezing-thawing and wetting-drying effects on polypropylene fiber reinforced metakaolin based geopolymer composites, Construct. Build. Mater. 235 (2020), https://doi.org/10.1016/j.conbuildmat.2019.117502.
[57] P. Behera, V. Baheti, J. Militky, S. Naeem, Microstructure and mechanical properties of carbon microfiber reinforced geopolymers at elevated temperatures, Construct. Build. Mater. 160 (2018) 733–743, https://doi.org/10.1016/j.conbuildmat.2017.11.109.
[58] S. Samal, Effect of high temperature on the microstructural evolution of fiber reinforced geopolymer composite, Heliyon 5 (2019), e01779, https://doi.org/10.1016/j.heliyon.2019.e01779.
[59] S. Samal, N. Phan Thanh, I. Petríková, B. Marvalová, Improved mechanical properties of various fabric-reinforced geocomposite at elevated temperature, JOM 67 (2015) 1478–1485, https://doi.org/10.1007/s11837-015-1420-x.
[60] G. Masi, W.D.A. Rickard, M.C. Bignozzi, A. Van Riessen, The effect of organic and inorganic fibres on the mechanical and thermal properties of aluminate activated geopolymers, Compos. B Eng. 76 (2015) 218–228, https://doi.org/10.1016/j.compositesb.2015.02.023.
[61] F.U.A. Shaikh, A. Hosan, Mechanical properties of steel fibre reinforced geopolymer concretes at elevated temperatures, Construct. Build. Mater. 114 (2016) 15–28, https://doi.org/10.1016/j.conbuildmat.2016.03.158.
[62] ASTM C618-17a, Standard Specification for Coal Fly Ash and Raw or Calcined Natural Pozzolan for Use in Concrete, ASTM International, West Conshohocken, PA, 2017.
[63] D. Zhang, J. Yu, H. Wu, B. Jaworska, B.R. Ellis, V.C. Li, Discontinuous micro-fibers as intrinsic reinforcement for ductile Engineered Cementitious Composites (ECC), Compos. B Eng. 184 (2020), https://doi.org/10.1016/j.compositesb.2020.107741.
[64] ASTM C1437-20, Standard Test Method for Flow of Hydraulic Cement Mortar, ASTM International, West Conshohocken, PA, 2020, www.astm.org, (n.d.).
[65] ASTM E831-19, Standard Test Method for Linear Thermal Expansion of Solid Materials by Thermomechanical Analysis, ASTM International, West Conshohocken, PA, 2019 (n.d.), www.astm.org.
[66] B. Chen, J. Liu, Residual strength of hybrid-fiber-reinforced high-strength concrete after exposure to high temperatures, Cement Concr. Res. 34 (2004) 1065–1069, https://doi.org/10.1016/j.cemconres.2003.11.010.
[67] X. Liang, C. Wu, Y. Su, Z. Chen, Z. Li, Development of ultra-high performance concrete with high fire resistance, Construct. Build. Mater. 179 (2018) 400–412, https://doi.org/10.1016/j.conbuildmat.2018.05.241.
[68] H.J. Yim, S.J. Park, J.H. Kim, H.G. Kwak, Nonlinear ultrasonic method to evaluate residual mechanical properties of thermally damaged concrete, ACI Mater. J. 111 (2014) 399–409, https://doi.org/10.14359/51686596.
[69] ASTM C109/C109M-20b, Standard Test Method for Compressive Strength of Hydraulic Cement Mortars (Using 2-in. Or [50 Mm] Cube Specimens), ASTM Int., 2020. https://www.astm.org/Standards/C109. (Accessed 5 August 2021).
[70] Japan Society of Civil Engineers, Recommendations for Design and Construction of High Performance Fiber Reinforced Cement Composites with Multiple Fine Cracks (HPFRCC), Concr. Eng. Ser. 82, 2008. Testing Method 6-10, http://www.jsce.or.jp/committee/concrete/e/index.html.
[71] V.F.F. Barbosa, K.J.D. MacKenzie, Synthesis and thermal behaviour of potassium sialate geopolymers, Mater. Lett. 57 (2003) 1477–1482, https://doi.org/10.1016/S0167-577X(02)01009-1.
[72] K. Meyer, P. Klobes, Comparison between different presentations of pore size distribution in porous materials, Fresenius' J. Anal. Chem. 363 (1999) 174–178, https://doi.org/10.1007/s002160051166.
[73] P. Krivenko, G. Kovalchuk, A. Palomo, A. FernÁndez-JimÉnez, Fly ash based geocements: genesis of microstructure and properties at hydration-dehydration process, Brittle Matrix Compos. 8 (2007) 55–64, https://doi.org/10.1533/9780857093080.55.
[74] P. Duxson, A.E. Grant, C.L. Ae, J.S.J. Van Deventer, Physical evolution of Na-geopolymer derived from metakaolin up to 1000 °C, (n.d.). https://doi.org/10.1007/s10853-006-0535-4.
[75] F.U.A. Shaikh, Effects of slag content on the residual mechanical properties of ambient air-cured geopolymers exposed to elevated temperatures, J. Asian Ceram. Soc. 6 (2018) 342–358, https://doi.org/10.1080/21870764.2018.1529013.
[76] Y. Li, Y. Zhang, E.H. Yang, K.H. Tan, Effects of geometry and fraction of polypropylene fibers on permeability of ultra-high performance concrete after heat exposure, Cement Concr. Res. 116 (2019) 168–178, https://doi.org/10.1016/j.cemconres.2018.11.009.
[77] Y.S. Jenq, S.P. Shah, Crack propagation in fiber-reinforced concrete, Civ. Environ. Eng. 112 (1986) 19–34.
[78] Z.H. Yan, K. Venkatesh, W. Bo, C. Liang, Q.S. Liang, Comparative thermal and mechanical performance of geopolymers derived from metakaolin and fly ash, J. Mater. Civ. Eng. 28 (2016), 4015092, https://doi.org/10.1061/(ASCE)MT.1943-5533.0001359.
[79] Z. Lafhaj, M. Goueygou, A. Djerbi, M. Kaczmarek, Correlation between porosity, permeability and ultrasonic parameters of mortar with variable water/cement ratio and water content, Cement Concr. Res. 36 (2006) 625–633, https://doi.org/10.1016/J.CEMCONRES.2005.11.009.
[80] G. Trtnik, F. Kavčič, G. Turk, Prediction of concrete strength using ultrasonic pulse velocity and artificial neural networks, Ultrasonics 49 (2009) 53–60, https://doi.org/10.1016/J.ULTRAS.2008.05.001.
[81] S.A. Omer, R. Demirboga, W.H. Khushefati, Relationship between compressive strength and UPV of GGBFS based geopolymer mortars exposed to elevated temperatures, Construct. Build. Mater. 94 (2015) 189–195, https://doi.org/10.1016/J.CONBUILDMAT.2015.07.006.
[82] R. Ghosh, S.P. Sagar, A. Kumar, S.K. Gupta, S. Kumar, Estimation of geopolymer concrete strength from ultrasonic pulse velocity (UPV) using high power pulser, J. Build. Eng. 16 (2018) 39–44, https://doi.org/10.1016/J.JOBE.2017.12.009.
[83] A. Noushini, A. Castel, The effect of heat-curing on transport properties of low-calcium fly ash-based geopolymer concrete, Construct. Build. Mater. 112 (2016) 464–477, https://doi.org/10.1016/J.CONBUILDMAT.2016.02.210.
[84] S.F.U. Ahmed, H. Mihashi, A review on durability properties of strain hardening fibre reinforced cementitious composites (SHFRCC), Cem. Concr. Compos. 29 (2007) 365–376, https://doi.org/10.1016/j.cemconcomp.2006.12.014.
[85] B. Nematollahi, S.M. Asce, J. Sanjayan, F. Uddin, A. Shaikh, Tensile Strain Hardening Behavior of PVA Fiber-Reinforced Engineered Geopolymer Composite, 2015, https://doi.org/10.1061/(ASCE)MT.1943-5533.
[86] Y. Zhao, T. Shi, L. Cao, L. Kan, M. Wu, Influence of steel slag on the properties of alkali-activated fly ash and blast-furnace slag based fiber reinforced composites, Cem. Concr. Compos. 116 (2021), 103875, https://doi.org/10.1016/j.cemconcomp.2020.103875.
[87] M. Magalhães, R. Toledo Filho, E. Fairbairn, Durability under thermal loads of polyvinyl alcohol fibers, Materia 18 (2013) 1587–1595, https://doi.org/10.1590/S1517-70762013000400018.
[88] S. Wang, V.C. Li, Engineered cementitious composites with high-volume fly ash, ACI Mater. J. 104 (2007) 233–241, https://doi.org/10.14359/18668.
[89] H. Schneider, J. Schreuer, B. Hildmann, Structure and properties of mullite—a review, J. Eur. Ceram. Soc. 28 (2008) 329–344, https://doi.org/10.1016/j.jeurceramsoc.2007.03.017.
[90] W.A. Deer Frs, R.A. Howie, J. Zussman, An Introduction to the Rock-Forming Minerals, 2013, https://doi.org/10.1180/DHZ.
[91] S.A. Bernal, J.L. Provis, B. Walkley, R. San Nicolas, J.D. Gehman, D.G. Brice, A. R. Kilcullen, P. Duxson, J.S.J. Van Deventer, Gel nanostructure in alkali-activated binders based on slag and fly ash, and effects of accelerated carbonation, Cement

Concr. Res. 53 (2013) 127–144, https://doi.org/10.1016/J.CEMCONRES.2013.06.007.
[92] P.V. Krivenko, G.Y. Kovalchuk, Directed synthesis of alkaline aluminosilicate minerals in a geocement matrix, J. Mater. Sci. 42 (2007) 2944–2952, https://doi.org/10.1007/s10853-006-0528-3.
[93] I. Ismail, S.A. Bernal, J.L. Provis, R. San Nicolas, S. Hamdan, J.S.J. Van Deventer, Modification of phase evolution in alkali-activated blast furnace slag by the incorporation of fly ash, Cem. Concr. Compos. 45 (2014) 125–135, https://doi.org/10.1016/J.CEMCONCOMP.2013.09.006.
[94] S.-D. Wang, K.L. Scrivener, Hydration products of alkali activated slag cement, Cement Concr. Res. 25 (1995) 561–571, https://doi.org/10.1016/0008-8846(95)00045-E.
[95] C. Alonso, L. Fernandez, Dehydration and rehydration processes of cement paste exposed to high temperature environments, J. Mater. Sci. 39 (2004) 3015–3024, https://doi.org/10.1023/B:JMSC.0000025827.65956.18.
[96] F. Li, L. Liu, Z. Yang, S. Li, Physical and mechanical properties and micro characteristics of fly ash-based geopolymer paste incorporated with waste Granulated Blast Furnace Slag (GBFS) and functionalized Multi-Walled Carbon Nanotubes (MWCNTs), J. Hazard Mater. 401 (2021), 123339, https://doi.org/10.1016/j.jhazmat.2020.123339.
[97] X. Zhao, C. Liu, L. Wang, L. Zuo, Q. Zhu, W. Ma, Physical and mechanical properties and micro characteristics of fly ash-based geopolymers incorporating soda residue, Cem. Concr. Compos. 98 (2019) 125–136, https://doi.org/10.1016/j.cemconcomp.2019.02.009.
[98] X. Jiang, R. Xiao, M. Zhang, W. Hu, Y. Bai, B. Huang, A laboratory investigation of steel to fly ash-based geopolymer paste bonding behavior after exposure to elevated temperatures, Construct. Build. Mater. 254 (2020), 119267, https://doi.org/10.1016/j.conbuildmat.2020.119267.
[99] R. Carl, L.V. C, W. Cynthia, H. Hideki, S. Tadashi, O. Atsuhisa, Measuring and modifying interface properties of PVA fibers in ECC matrix, J. Mater. Civ. Eng. 13 (2001) 399–406, https://doi.org/10.1061/(ASCE)0899-1561(2001)13:6(399).
[100] J. Luo, Z. Cai, K. Yu, W. Zhu, Z. Lu, Temperature impact on the micro-structures and mechanical properties of high-strength engineered cementitious composites, Construct. Build. Mater. 226 (2019) 686–698, https://doi.org/10.1016/j.conbuildmat.2019.07.322.
[101] K.D. Hertz, Concrete strength for fire safety design, Mag. Concr. Res. 57 (2005) 445–453, https://doi.org/10.1680/macr.2005.57.8.445.